

# The Crustal Stress Field of Germany - A Refined Prediction

**Steffen Ahlers** (✉ [ahlers@geo.tu-darmstadt.de](mailto:ahlers@geo.tu-darmstadt.de))

Institute of Applied Geosciences <https://orcid.org/0000-0001-9094-0116>

**Luisa Röckel**

Karlsruher Institut für Technologie

**Tobias Hergert**

Technische Universität Darmstadt

**Karsten Reiter**

Technische Universität Darmstadt

**Oliver Heidbach**

Deutsches Geoforschungszentrum Potsdam

**Andreas Henk**

Technische Universität Darmstadt

**Birgit Müller**

Karlsruher Institut für Technologie

**Sophia Morawietz**

Deutsches Geoforschungszentrum Potsdam

**Magdalena Scheck-Wenderoth**

Deutsches Geoforschungszentrum Potsdam

**Denis Anikiev**

Deutsches Geoforschungszentrum Potsdam

---

## Research Article

**Keywords:** 3D geomechanical–numerical model, Stress tensor, Stress magnitudes, Stress state, Upper Rhine Graben, North German Basin, Molasse Basin, Germany

**Posted Date:** December 13th, 2021

**DOI:** <https://doi.org/10.21203/rs.3.rs-1128920/v1>

**License:**  This work is licensed under a Creative Commons Attribution 4.0 International License.

[Read Full License](#)

---

1 **Title:** The crustal stress field of Germany - A refined prediction

2 Steffen Ahlers<sup>1</sup>, Luisa Röckel<sup>2</sup>, Tobias Hergert<sup>1</sup>, Karsten Reiter<sup>1</sup>, Oliver Heidbach<sup>3,4</sup>, Andreas  
3 Henk<sup>1</sup>, Birgit Müller<sup>2</sup>, Sophia Morawietz<sup>3,4</sup>, Magdalena Scheck-Wenderoth<sup>5,6</sup>, Denis Anikiev<sup>5</sup>

4 <sup>1</sup>Engineering Geology, Institute of Applied Geosciences, TU Darmstadt, 64287 Darmstadt, Germany

5 <sup>2</sup>Technical Petrophysics, Institute of Applied Geosciences, KIT, 76131 Karlsruhe, Germany

6 <sup>3</sup>Seismic Hazard and Risk Dynamics, GFZ German Research Centre for Geosciences, 14473 Potsdam, Germany

7 <sup>4</sup>Institute for Applied Geosciences, TU Berlin, 10587 Berlin, Germany

8 <sup>5</sup>Basin Modelling, GFZ German Research Centre for Geosciences, 14473 Potsdam, Germany

9 <sup>6</sup>Department of Geology, Geochemistry of Petroleum and Coal, Faculty of Georesources and Material  
10 Engineering, RWTH Aachen University, Aachen, Germany

11 **Corresponding author:** Steffen Ahlers (ahlers@geo.tu-darmstadt.de)

12 **Abstract:**

13 Information about the absolute stress state in the upper crust plays a crucial role in the planning and  
14 execution of e.g., directional drilling, stimulation and exploitation of geothermal and hydrocarbon  
15 reservoirs. Since many of these applications are related to sediments, we present a refined  
16 geomechanical-numerical model for Germany with focus on sedimentary basins, able to predict the  
17 complete 3D stress tensor. The lateral resolution of the model is 2.5 km, the vertical resolution about  
18 250 m. Our model contains 22 units with focus on the sedimentary layers parameterized with  
19 individual rock properties. The model results show an overall good fit with magnitude data of the  
20 minimum ( $S_{hmin}$ ) and maximum horizontal stress ( $S_{Hmax}$ ) that are used for the model calibration. The  
21 mean of the absolute stress differences between these calibration data and the model results is 4.6  
22 MPa for  $S_{hmin}$  and 6.4 MPa for  $S_{Hmax}$ . In addition, our predicted stress field shows good agreement to  
23 several supplementary in situ data from the North German Basin, the Upper Rhine Graben and the  
24 Molasse Basin.

25 **Keywords:** 3D geomechanical–numerical model, Stress tensor, Stress magnitudes, Stress  
26 state, Upper Rhine Graben, North German Basin, Molasse Basin, Germany

27

## 28 1 Introduction

29 The prediction of the recent crustal stress field is important for many applications regarding the  
30 exploitation or use of the subsurface, particularly for directional drilling, stimulation and exploitation  
31 of geothermal or hydrocarbon reservoirs. Another currently important application is the search for  
32 and long-term safety assessment of a high-level nuclear waste deposit. However, up to now the  
33 knowledge of the crustal stress field for Germany is limited. It is essentially based on two major  
34 databases regarding stress tensor orientations and stress magnitudes (Heidbach et al., 2016;  
35 Morawietz et al., 2020), several 2D numerical models (Grünthal and Stromeyer, 1994; Marotta et al.,  
36 2002; Kaiser et al., 2005; Jarosiński et al., 2006; Cacace et al., 2008) and some regional scale 3D  
37 geomechanical-numerical models (Buchmann and Connolly, 2007; Heidbach et al., 2014; Hergert et  
38 al., 2015; Ziegler et al., 2016). The only large scale 3D model that covers entire Germany has been  
39 presented by Ahlers et al. (2021a). However, this model focuses on the large-scale stress pattern in  
40 the entire crust with low resolution in sediments that are represented with homogeneous mean rock  
41 properties.

42 To take a further step towards a robust prediction of the recent crustal stress state, we developed a  
43 geomechanical-numerical model of Germany based on Ahlers et al. (2021a). It provides a continuous  
44 prediction of the crustal stress in 3D with focus on the sedimentary basins. The work of Ahlers et al.  
45 (2021a) also provided a continuous description of the stress state of Germany but focused on  
46 basement structures and included a homogenous sedimentary layer without mechanical  
47 stratification in a coarse resolution. The model presented here has been significantly improved with a  
48 differentiated sedimentary layer, consisting of 15 units with specific material properties (density,  
49 Poisson's ratio and Young's modulus) and an eighteen-time higher resolution in the upper part of the  
50 crust. An improved differentiation of the sedimentary layer is essential since the majority of  
51 applications focuses on sedimentary basins particularly for geothermal and hydrocarbon  
52 exploitation. At the same time, stress conditions within sedimentary units can be particularly  
53 challenging due to structural, lithological and mechanical variability. Mechanical properties varying

54 with depth - mainly stiffness contrasts – can lead to differing stress magnitudes, differential stresses  
55 and perturbations in the orientation of the maximum horizontal stress ( $S_{Hmax}$ ) (Cornet and Röckel,  
56 2012; Heidbach et al., 2014; Hergert et al., 2015). Extreme cases include very weak layers of salt or  
57 clay, leading to a nearly lithostatic stress state, which can mechanical decouple the overburden from  
58 the underburden layers (Roth and Fleckenstein, 2001; Röckel and Lempp, 2003; Heidbach et al.,  
59 2007; Ahlers et al., 2019). Furthermore, our new model is calibrated with minimum horizontal stress  
60 ( $S_{hmin}$ ) magnitudes which significantly improve the reliability of the predicted stress state compared  
61 to the model Ahlers et al. (2021a), which could only be calibrated with  $S_{hmin}$  values.

## 62 2 Model setup

### 63 2.1 Method

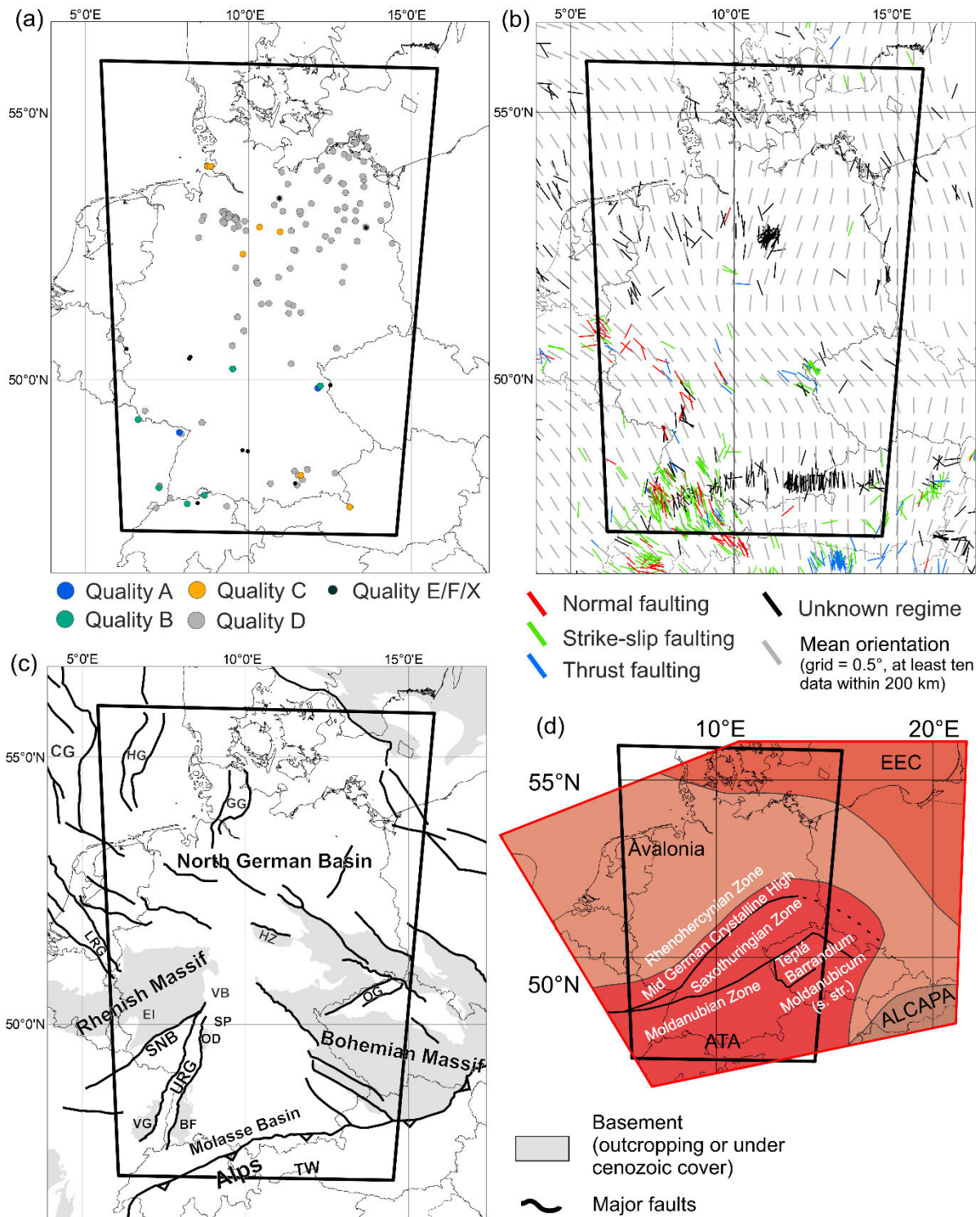
64 We assume linear elasticity and use the finite element method to solve the partial differential  
65 equations of the equilibrium of forces. First, an appropriate initial stress state is defined representing  
66 an undisturbed state of stress governed by gravity. In a second step, the stress state in the model is  
67 calibrated with magnitude data by varying displacement boundary conditions defined at the model  
68 edges. This modeling approach has been used for different tectonic settings and scales and is  
69 described in detail in Buchmann and Connolly (2007), Hergert and Heidbach (2011), Heidbach et al.  
70 (2014), Reiter and Heidbach (2014), Hergert et al. (2015) and Ahlers et al. (2021a). For the  
71 construction and discretization of the 3D model geometry and the assignment of rock properties to  
72 individual finite elements the software packages GOCAD™, HyperMesh™ and ApplePY (Ziegler et al.,  
73 2019) are used. As solver, we use the commercial finite element software package Abaqus™ v2019.  
74 For post-processing Tecplot 360™ enhanced with the GeoStress add-on (Stromeyer and Heidbach,  
75 2017) is used.

### 76 2.2 Geology of the study area

77 The diverse history of the model area lead to the complex geological structure observed today  
78 (Figure 1c, d). The upper crust can be subdivided into four parts: the East European Craton (EEC) in

79 the northeast amalgamated with Avalonia further south during the Caledonian orogeny, the  
80 Armorican Terrane Assemblage (ATA) added during the Variscan orogeny and finally the Alp-  
81 Carpathian-Pannonian (ALCAPA) part as a result of the Alpine orogeny (Ziegler and Dèzes, 2006;  
82 McCann, 2008; Linnemann and Romer, 2010). Since these units are identical to Ahlers et al. (2021a)  
83 we refer to this publication for further information. The basement of the model area is mainly  
84 covered by late Paleozoic to Cenozoic sediments, with the exception of the Rhenish and Bohemian  
85 massifs commonly interpreted as long-lived highs (e.g., Eynatten et al., 2021), the Alpine mountain  
86 chain and parts of the Mid German Crystalline High (MGCH) and Moldanubian Zone (MDZ). During  
87 the final phase of the Variscan orogeny from the late Carboniferous to Permian time the model area  
88 was affected by extension leading to the origin of several basins filled up with debris of the eroding  
89 Variscan orogeny and contemporaneous volcanic activity mainly located in NE Germany (McCann et  
90 al., 2008; Scheck-Wenderoth et al., 2008). Due to the large amount of mostly reddish clastic and  
91 volcanic rocks deposited, this time period is called Rotliegend. The largest basin developed was the  
92 Southern Permian Basin with a maximum extent of ~1700 km covering large areas of the northern  
93 model area (Stollhofen et al., 2008). During the late Permian, this basin was flooded from the north  
94 leading to the deposition of the so-called 'Zechstein' evaporites (McCann et al., 2008). The following  
95 Triassic development of the model area was controlled by the breakup of Pangea and the westward  
96 opening of the Tethys leading to an E-W dominated extensional tectonic regime and the  
97 development of N-S oriented graben systems mainly in the north e.g., the Central Graben or the  
98 Glückstadt Graben (Figure 1c) (Scheck-Wenderoth and Lamarche, 2005; Kley et al., 2008). During this  
99 time period the southern 'Alpine' part of the model area was characterized by open marine  
100 conditions of the Tethys shelf, whereas continental to shallow marine conditions by repeated  
101 incursions of the Tethys dominated the northern 'Germanic' domain (Feist-Burkhardt et al., 2008).  
102 The Jurassic was dominated by the progressive breakup of Pangea and mostly marine conditions  
103 (Pienkowski et al., 2008). Central Europe was still affected by extensional tectonics but the extension  
104 direction changed to NW-SE during the Late Jurassic (Kley et al., 2008). During the Early Cretaceous

105 this development continued with depocenters in the northern part of the model area (Voigt et al.,  
106 2008). However, the deposition of sediments was restricted to these depocenters that evolved as an  
107 echelon subbasins along the southern margin of the Permian Basin in a transtensional regime  
108 (Scheck-Wenderoth et al., 2008).The largest part of the former Permian Basin area in the northern  
109 domain of the model area was uplifted during Late Jurassic to Early Cretaceous times. In the Late  
110 Cretaceous the tectonic setting and depositional conditions changed. Due to an eustatic sea-level rise  
111 large parts of Central Europe were flooded and predominantly carbonates and sandstones were  
112 deposited (Scheck-Wenderoth et al., 2008). The rotation of Iberia reversed the tectonic regime  
113 leading to the inversion of former depocenters, the formation of thrust faults and basement uplifts  
114 e.g., the Harz mountains (Kley et al., 2008). Additional processes for the Late Cretaceous to  
115 Paleogene exhumation are still discussed (Eynatten et al., 2021). The Cenozoic development of the  
116 model area was mainly influenced by the collision of Africa and Eurasia leading to the rise of the  
117 Alpine mountain chains and the evolution of the Molasse Basin (MB). In addition, the Cenozoic Rift  
118 System developed e.g., the Upper Rhine Graben (URG) and the Lower Rhine Graben (LRG) (Ziegler  
119 and Dèzes, 2006) and the uplift of the Rhenish Massif began (Reicherter et al., 2008). Except the  
120 sedimentary basins of the MB, the URG, the LRG and the North German Basin (NGB) large parts of  
121 the model area were affected by erosion (Rasser et al., 2008). The Cenozoic tectonics north of the  
122 Alps were accompanied by various volcanic activities e.g., the Vogelsberg Complex, the Eifel, Ohře  
123 Graben or in the vicinity of the URG (Litt et al., 2008; Reicherter et al., 2008).



124

125 Figure 1: Overview of the geology of the model region and stress data used for comparison and calibration. The black frame  
 126 shows the key area of the model with increased stratigraphic resolution based on Anikiev et al. (2019). (a) Distribution of  
 127 the stress magnitude data of Morawietz and Reiter (2020). The color-coded dots indicate the quality assigned by Morawietz  
 128 et al. (2020). Displayed are all data from a true vertical depth (TVD) >200 m. (b) Data of the World Stress Map (WSM) of  
 129 Heidbach et al. (2016) and Levi et al. (2019). Color-coded lines indicate the stress regime and the orientation of  $S_{Hmax}$ . Grey  
 130 lines show the mean orientation of  $S_{Hmax}$  on a regular grid (Details see chapter 3.1). (c) Geological framework of the model  
 131 area based on Asch (2005) and Kley and Voigt (2008). BF – Black Forest, CG – Central Graben, EI – Eifel, HG – Horn Graben,  
 132 HZ – Harz Mountains, GG – Glückstadt Graben, LRG – Lower Rhine Graben, OD – Odenwald, OG – Ohře Graben, SNB –  
 133 Saar-Nahe Basin, SP – Spessart, TW – Tauern Window, URG – Upper Rhine Graben, VB – Vogelsberg Complex, VG – Vosges.  
 134 (d) Overview of the basement structures based on Kroner et al. (2010) and Brückl et al. (2010). The red frame shows the  
 135 entire model area. ALCAPA - Alps-Carpathian-Pannonian, ATA - Armorican Terrane Assemblage, EEC - East European Craton.

### 136 2.3 Model geometry

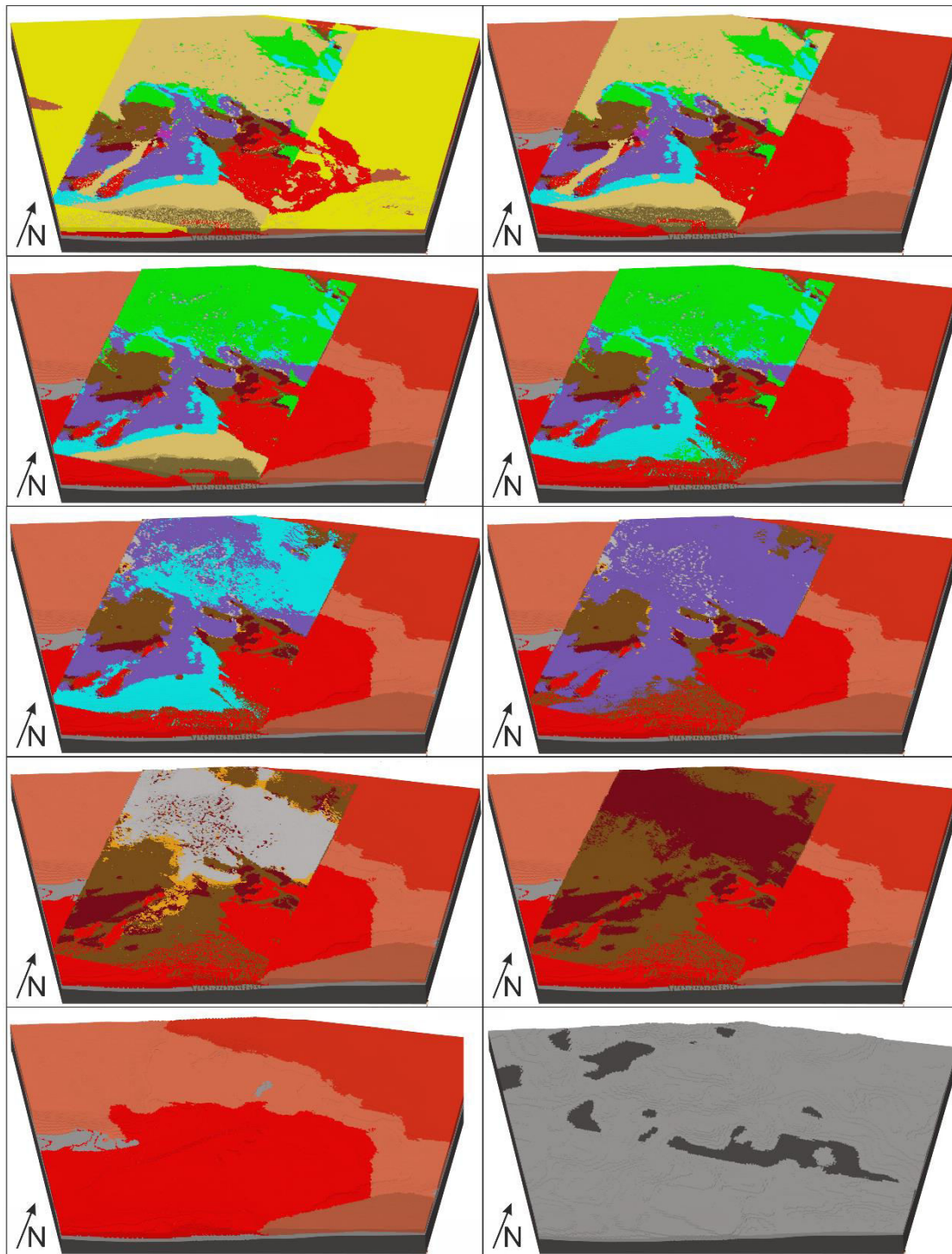
137 All basic information about the model area and geometry is described in Ahlers et al. (2021a).  
138 However, in order to refine the resolution w.r.t. to the former model we subdivide the sediment  
139 layer. The subdivision is based on the 3D-Deutschland (3DD) model of Anikiev et al. (2019) and is  
140 therefore only resolved in the key area of our model (Figure 2). We did not extend the higher  
141 stratigraphic resolution to the whole model area since the data availability is poor and our focus area  
142 is covered by the 3DD data. Thus, the sedimentary units outside of the 3DD area are combined to a  
143 single unit. Furthermore, the stress data used for calibration are mainly located within the 3DD  
144 model area. The geometry data include a gap between the base of the Rotliegend - the deepest layer  
145 almost completely contained in the 3DD model - and the surface of the crystalline basement of  
146 Ahlers et al. (2021a). All lithological units between are represented by one unit named Pre-Permian  
147 unit though we aware that this is a very heterogeneous unit comprising early- to mid-Paleozoic low-  
148 grade metamorphic sediments and late-Paleozoic sediments.

### 149 2.4 Model discretization

150 The average lateral resolution of the model is 2.5 km and constant over the entire depth range of the  
151 model, the vertical resolution varies with depth. The mesh is divided into three vertical zones with a  
152 decreasing resolution with increasing depth. The deepest and most coarsely resolved unit is the  
153 lithospheric mantle limited by the bottom of the model and the Mohorovičić discontinuity with five  
154 element layers leading to a vertical resolution of 10 to 15 km. The mesh of the crust is subdivided at  
155 10 km depth. Below 10 km depth the mesh contains ten element layers with a vertical resolution  
156 between 2.5 and 4 km. Above 10 km depth the mesh contains 43 element layers with a vertical  
157 resolution of about 240 m. Overall, the mesh contains about 11.1 million hexahedral elements.

158 Due to the complex geometry of the individual layers, especially of the sedimentary units, we did not  
159 create an individual mesh for each of them. We use ApplePY (Ziegler et al., 2019) to assign the  
160 individual mechanical properties of each unit to the finite elements of the mesh. Therefore apart

161 from the lithospheric mantle, which is the deepest meshed zone, the geometry of the individual units  
162 are not directly represented by the mesh. The final model consists of 22 units (Table 1): the  
163 lithospheric mantle, the lower crust, four units of the upper crust (EEC, Avalonia, ATA, ALCAPA), the  
164 Pre-Permian unit, Rotliegend volcanics and sediments, Zechstein carbonates and salt, Mesozoic units  
165 of the Triassic, Jurassic and Cretaceous, thrust units of the Alps, folded units of the MB, three  
166 lateral subdivided units of Cenozoic sediments (NGB, URG and MB), Cenozoic volcanics and the  
167 sediments outside the 3DD area. Additionally, there are some relict elements (Table 1, Layer ID: 2)  
168 which arise from the element assignment with ApplePY if the surface of the mesh does not fit  
169 perfectly to the surface defined by the geometry used. This occurs because the geometry of the 3DD  
170 model has a higher resolution (1 x 1 km) than the mesh of our model (~2.5 x 2.5 km).



171

172 Figure 2: Overview of the discretized model showing the internal structure including 22 units. ATA - Armorican Terrane  
 173 Assemblage, ALCAPA - Alpine-Carpathian-Pannonian, EEC - East European Craton, NGB - North German Basin, URG - Upper  
 174 Rhine Graben.

## 175 2.5 Rock properties

176 Individual material properties are assigned to all 22 units of the model (Table 1). The density and the  
177 elastic properties (Young's modulus and Poisson's ratio) are defined as material properties for the  
178 numerical calculation, i.e. linear-elastic material behavior is assumed. Friction angle, cohesion and  
179 tensile strength are only used for post-processing analysis later on. Although our model contains 22  
180 units, the Triassic and Jurassic units still contain mechanically very different subunits. For example,  
181 the Triassic unit comprises the sandstone-dominated Buntsandstein, the carbonate- and evaporate-  
182 dominated Muschelkalk and the claystone-dominated Keuper (Feist-Burkhardt et al., 2008).  
183 Therefore, we calculated the arithmetic mean of the subunits for the mechanical properties of these  
184 two units. Another challenge was the parametrization of the thrust units of the Alps, the  
185 sediments outside the 3DD area and the relict elements unit. Since the relict elements can only occur  
186 at the top of the model, we used an average value of the three Cenozoic sedimentary units (NGB,  
187 URG and MB). For the sediments outside of the 3DD model area, we have chosen roughly estimated  
188 values. For the thrust units of the Alps, we decided to use the mean of the Mesozoic units with the  
189 exception of the density. As for almost all other units, we use the density values from the 3DD model  
190 of Anikiev et al. (2019). The elastic properties are mainly based on the P<sup>3</sup> database (Bär et al., 2020)  
191 and Hergert et al. (2015). In addition, the friction angle and cohesion are mainly based on the latter.  
192 The tensile strength is assumed to be 5 MPa for almost all units, since available data are limited. In  
193 general, all values in Table 1 without a reference are roughly estimated. The friction angle, cohesion  
194 and tensile strength of the Zechstein salt are not defined due to the visco-elastic properties of salt  
195 (e.g., Urai et al., 2008). In addition, we defined a Young's modulus gradient for all units with the  
196 exception of the sediments outside 3DD as it led to convergence problems at the model edges. The  
197 Young's modulus gradient should mimic the tendency of the rock mass to strengthen with increasing  
198 depth due to compaction and increasing confining pressure. An effect that can be seen, for example,  
199 in the decrease of porosity and permeability with increasing depth (Ingebritsen and Manning, 1999).  
200 Our Young's modulus gradient reaches from 1.5 km depth to the surface, describing a reduction of

201 the Young's modulus from 100 % (of the values in Table 1) to 10 % at the surface. The reduction to  
 202 10% is derived from Hudson and Harrison (1997) and the depth of the gradient was iterated by  
 203 preliminary tests.

204 Table 1: Overview of all units defined in the model and parameters used. For abbreviations, see  
 205 Figure 2.

Layer ID	Name	Density [kg/m <sup>3</sup> ]	Young's modulus [GPa]	Poisson's ration [-]	Friction angle [°]	Cohesion [MPa]	Tensile Strength [MPa]
2	Relict elements	2400 <sup>a</sup>	15 <sup>b</sup>	0.29 <sup>b</sup>	38 <sup>b</sup>	10 <sup>b</sup>	5
3	Sediments outside 3DD	2700	30	0.25	38 <sup>b</sup>	10 <sup>b</sup>	5
4	Cenozoic volcanics	2860 <sup>a</sup>	54 <sup>c</sup>	0.25 <sup>c</sup>	50 <sup>i</sup>	39 <sup>i</sup>	5
5	Cenozoic sediments of the NGB	2480 <sup>a</sup>	15 <sup>b</sup>	0.29 <sup>b</sup>	38 <sup>b</sup>	10 <sup>b</sup>	5
6	Cenozoic sediments of the URG	2300 <sup>a</sup>	15 <sup>b</sup>	0.29 <sup>b</sup>	38 <sup>b</sup>	10 <sup>b</sup>	5
7	Cenozoic sediments of the Molasse Basin	2350 <sup>a</sup>	15 <sup>b</sup>	0.29 <sup>b</sup>	38 <sup>b</sup>	10 <sup>b</sup>	5
8	Folded Molasse	2400 <sup>a</sup>	15 <sup>b</sup>	0.29 <sup>b</sup>	38 <sup>b</sup>	10 <sup>b</sup>	5
9	Thrusted units of the Alps	2700 <sup>a</sup>	23 <sup>c</sup>	0.25 <sup>c</sup>	40	25	5
10	Cretaceous	2590 <sup>a</sup>	20 <sup>c</sup>	0.25 <sup>c</sup>	40 <sup>j</sup>	18 <sup>j</sup>	7 <sup>k</sup>
11	Jurassic	2600 <sup>a</sup>	20 <sup>c</sup>	0.26 <sup>c</sup>	36 <sup>b,j</sup>	15 <sup>b,j</sup>	5
12	Triassic	2650 <sup>a</sup>	28 <sup>c</sup>	0.25 <sup>c</sup>	36 <sup>b,j</sup>	31 <sup>b,j</sup>	5
13	Zechstein salt	2100 <sup>a</sup>	25 <sup>g</sup>	0.27 <sup>g</sup>	-	-	-
14	Zechstein carbonates	2400 <sup>a</sup>	30 <sup>c</sup>	0.25 <sup>c</sup>	50 <sup>i</sup>	18 <sup>i</sup>	5
15	Rotliegend sediments	2600 <sup>a</sup>	15 <sup>c</sup>	0.19 <sup>c</sup>	43 <sup>l,m</sup>	25 <sup>l,m</sup>	5 <sup>l,m</sup>
16	Rotliegend volcanics	2650 <sup>a</sup>	26 <sup>c</sup>	0.25 <sup>c</sup>	40 <sup>l</sup>	57 <sup>l</sup>	15 <sup>l</sup>
17	Pre-Permian	2670 <sup>a</sup>	40 <sup>c</sup>	0.25 <sup>h</sup>	40 <sup>l,n</sup>	15 <sup>l,n</sup>	5 <sup>l,n</sup>
18	Upper crust ALCAPA	2750 <sup>d</sup>	70 <sup>h</sup>	0.25 <sup>h</sup>	40 <sup>b,c</sup>	30 <sup>b,c</sup>	5
19	Upper crust ATA	2790 <sup>e</sup>	70 <sup>h</sup>	0.25 <sup>h</sup>	40 <sup>b,c</sup>	30 <sup>b,c</sup>	5
20	Upper crust AV	2820 <sup>d</sup>	70 <sup>h</sup>	0.25 <sup>h</sup>	40 <sup>b,c</sup>	30 <sup>b,c</sup>	5
21	Upper crust EEC	2810 <sup>d</sup>	70 <sup>h</sup>	0.25 <sup>h</sup>	40 <sup>b,c</sup>	30 <sup>b,c</sup>	5
22	Lower crust	3000 <sup>d,e</sup>	80 <sup>h</sup>	0.25 <sup>h</sup>	40 <sup>b,c</sup>	30 <sup>b,c</sup>	5
1	Lithospheric mantle	3300 <sup>e,f</sup>	130	0.25 <sup>h</sup>	40 <sup>b,c</sup>	30 <sup>b,c</sup>	5

206 <sup>a</sup>Anikiev et al. (2019), <sup>b</sup>Hergert et al. (2015), <sup>c</sup>Bär et al. (2020), <sup>d</sup>Maystrenko and Scheck-Wenderoth (2013), <sup>e</sup>Tašárová et al.  
207 (2016), <sup>f</sup>Przybycin et al. (2015), <sup>g</sup>Wenting et al. (2017), <sup>h</sup>Turcotte and Schubert (2014), <sup>i</sup>Zoback (2007), <sup>j</sup>Reyer (2013),  
208 <sup>k</sup>Dubelaar and Nijland (2016), <sup>l</sup>Alber et al. (2015), <sup>m</sup>Stöckhert et al. (2013), <sup>n</sup>Alber and Solibida (2017).

## 209 2.6 Initial stress state

210 An initial stress state is established, describing an only gravity-driven undisturbed, non-tectonic  
211 stress field within the upper crust before the displacement boundary conditions are applied. To  
212 achieve such an initial stress state, we extend our model with a sideburden (dark blue), an  
213 underburden (light blue) and a stiff shell (green) (Figure 3a, b). The shell has a conic shape with a  
214 theoretical intersection point at the center of the earth emulating the naturally increasing confining  
215 pressure with depth (Zang and Stephansson, 2010). The elastic properties (Young's modulus and  
216 Poisson's ratio) of the sideburden and underburden are the adjusting screws to set a best-fit initial  
217 stress state. For calibration we use a semi-empirical function of Sheorey (1994) describing the  
218 undisturbed stress state of the earth as stress ratio (k):

$$219 \quad k = \frac{S_{Hmean}}{S_V} = \frac{S_{Hmax} + S_{Hmin}}{2S_V} \quad (1)$$

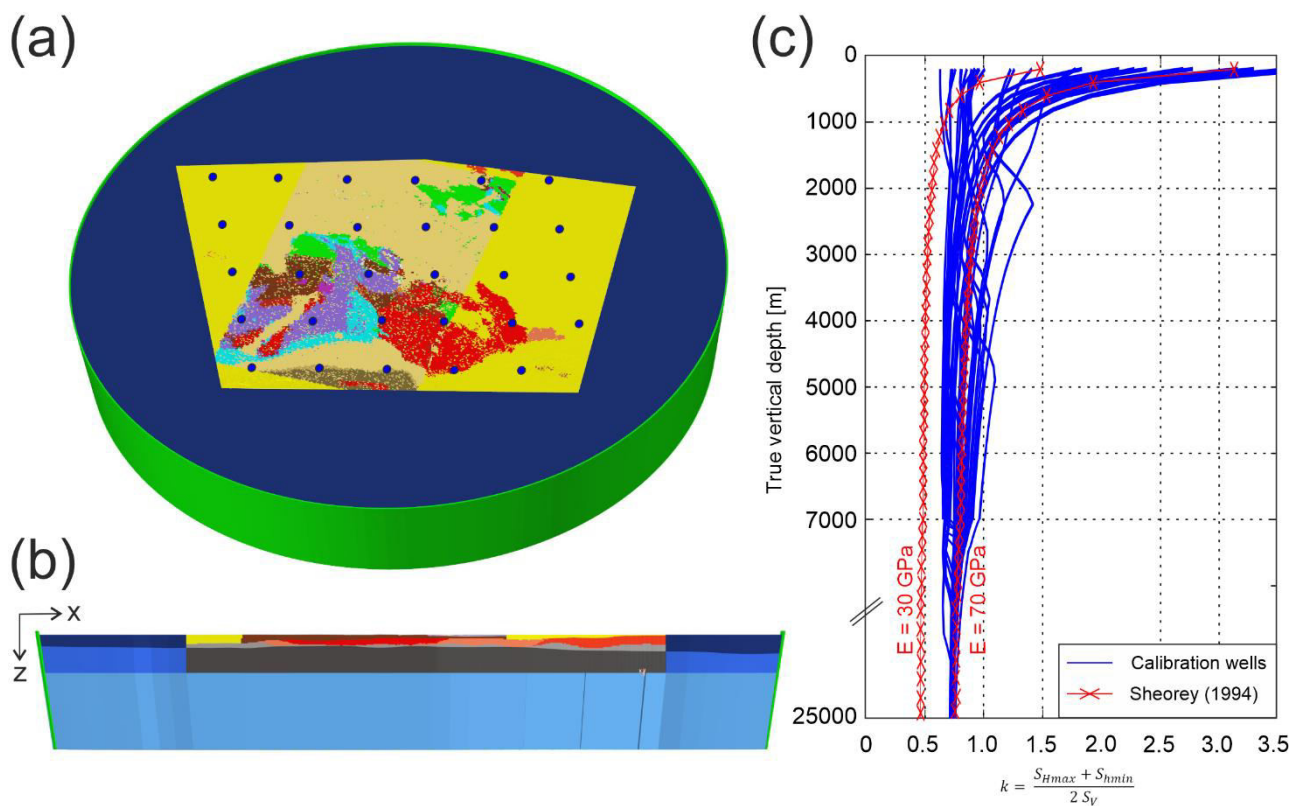
220 depending on depth (z) and Young's modulus (E):

$$221 \quad k = 0.25 + 7E \left( 0.001 + \frac{1}{z} \right) \quad (2)$$

222 we compare the theoretical k values with k values of our model using 29 virtual wells up to 25 km  
223 true vertical depth (TVD) (blue dots in Figure 2a). Subsequently, we vary the gravity-driven  
224 settlement of the model by varying the Young's modulus of the underburden and increase or  
225 decrease the influence of  $S_V$  on the horizontal stresses by varying the Poisson's ratio within the model  
226 and the sideburden. This workflow has been used and described in detail by several authors before  
227 e.g., Buchmann and Connolly (2007), Hergert (2009), Hergert and Heidbach (2011), Reiter and  
228 Heidbach (2014) or Ahlers et al. (2021a).

229 Our best-fit regarding the theoretical stress state of Sheorey (1994) is displayed in Figure 3c. There is  
230 a change of scale along the depth axis below 7000 m TVD since a uniform stress state and an almost  
231 perfect fit to the theoretical curve (red curve) is achieved at greater depths when all wells reach the

232 upper crustal units (Layer ID: 18 - 21) with a homogeneous Young's modulus of 70 GPa. About half of  
 233 the calibration wells (blue curves) show an almost vertical progression within the upper 1500 m,  
 234 while the other half follows the progression of the theoretical curve of Sheorey (1994) to higher  $k$   
 235 values with decreasing depth. This effect occurs due to the Young's modulus gradient defined within  
 236 the main area of our model up to 1500 m TVD. Figure 3c includes the function of Eq. (2) for a Young's  
 237 modulus of 30 GPa typical for the sediments and a Young's modulus of 70 GPa representing  
 238 crystalline basement units.



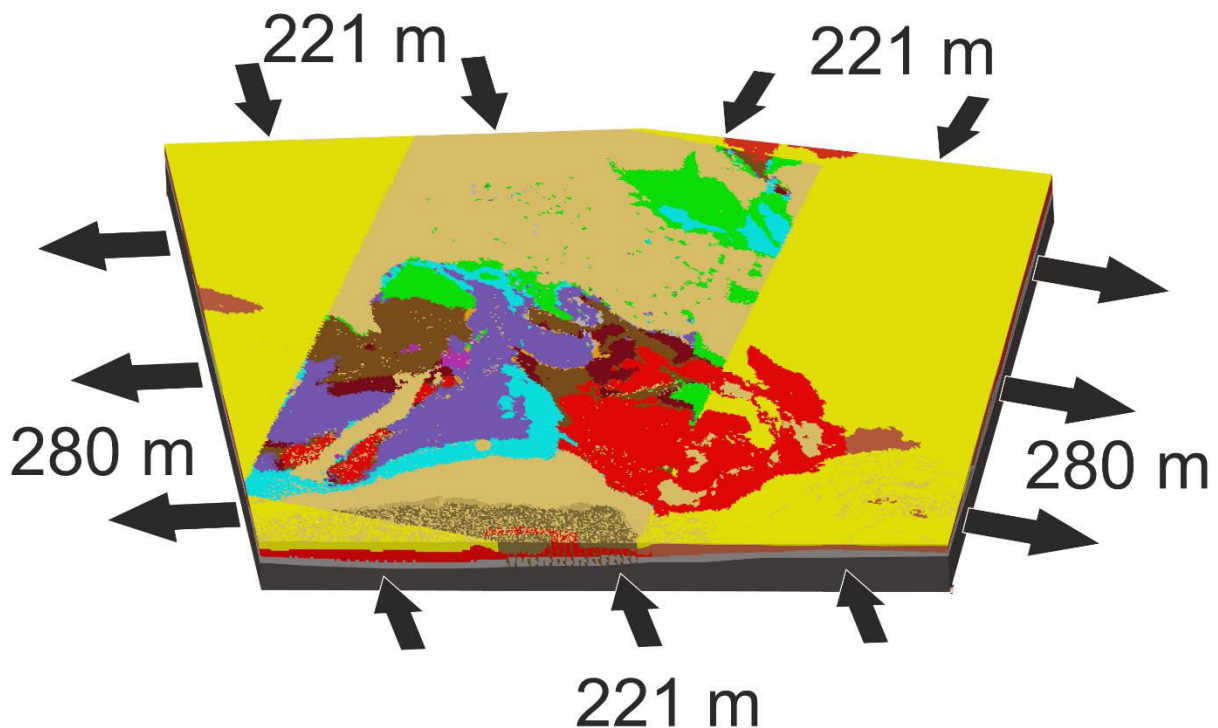
239

240 Figure 3: Top (a) and side view (b) of the extended model box used to achieve an initial stress state. (c) Best-fit of 29 virtual  
 241 wells (blue curves and blue dots in (a)) in comparison to calculated curves (red) for a Young's modulus of 30 and 70 GPa  
 242 based on Sheorey (1994). There is a change of the scale of the depth axis below 7000 m TVD.

## 243 2.7 Displacement boundary conditions and calibration

244 After the initial stress state is reached, the model is calibrated with measured in situ stress data using  
 245 variable displacement boundary conditions. The bottom of the model is fixed vertically, horizontal  
 246 displacements are allowed and the model surface is free. Displacement boundary conditions are  
 247 defined at the five vertical model edges (Figure 4). The directions of displacements are predefined by

248 the mean  $S_{Hmax}$  orientation derived from the *World Stress Map* (WSM, Heidbach et al., 2016) data  
249 (Figure 1b). At the northern and southern edges, where  $S_{Hmax}$  is oriented perpendicular to the model  
250 boundary, compression is applied. Accordingly, extension is applied at the western and eastern  
251 edges, where  $S_{Hmax}$  is parallel to the model boundary. The magnitudes of the displacement boundary  
252 conditions are derived through a calibration process using in-situ stress magnitudes from the  
253 database of Morawietz and Reiter (2020). Since  $S_v$  is based almost entirely on density and is not  
254 influenced by displacement boundary conditions applied, only the  $S_{Hmax}$  and  $S_{hmin}$  magnitudes are  
255 used for calibration. We use only data qualities from A to C and values from TVDs >200 m to  
256 minimize possible topographical effects. Thus, in total 73  $S_{hmin}$  and 56  $S_{Hmax}$  magnitudes from 200 to  
257 ~4700 m TVD are available from the database of Morawietz and Reiter (2020). Since the calibration  
258 data are unevenly distributed with depth (Figure 6 & Figure 8) a depth-weighted median for depth  
259 intervals of 500 m is used as decisive calibration value. The best-fit is achieved with a total shortening  
260 of 442 m in N-S direction and an extension of 560 m in E-W direction (Figure 4).

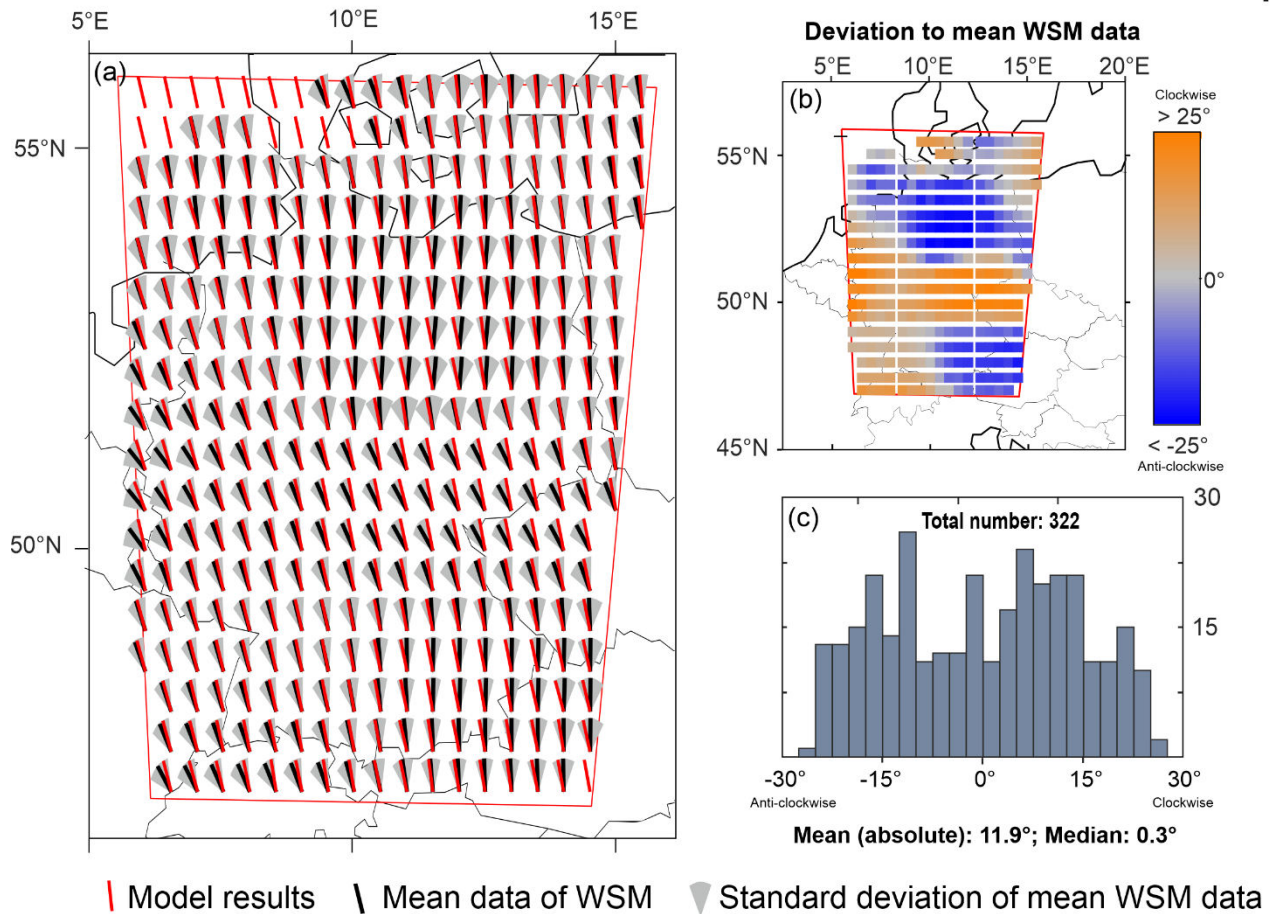


261

262 Figure 4: Displacement boundary conditions applied at the discretized model. Arrows indicate direction of the  
263 displacements applied, numbers the magnitudes of displacements defined for the best-fit.

264 3 Results

265 3.1 Orientation of  $S_{Hmax}$



266

267 Figure 5: Orientation of  $S_{Hmax}$  predicted by the model in comparison to the mean orientation of the WSM (Heidbach et al.,  
 268 2016) and Levi et al. (2019). Details are described in the text. (a) Model results at 5 km TVD (red lines), the mean  
 269 orientation derived from the WSM (black lines) with standard deviation (grey wedges). (b) Color-coded deviation between  
 270 the results and the mean orientation of the WSM. Blue indicates an anti-clockwise rotation of the model results and orange  
 271 a clockwise rotation of the model results w.r.t the mean orientation of the WSM. (c) Histogram showing the deviation  
 272 displayed in (a) and (b).

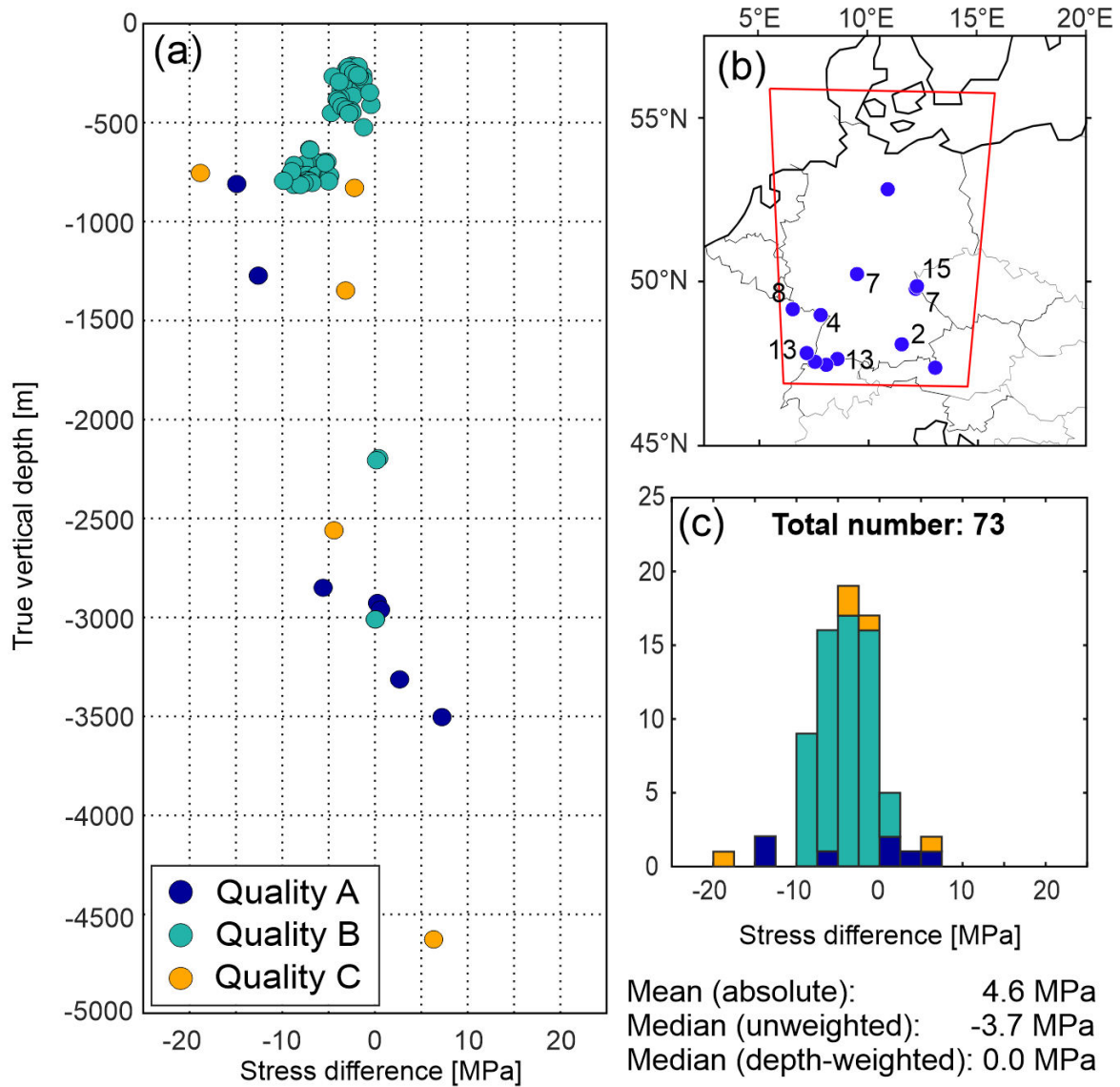
273 The orientations of  $S_{Hmax}$  in comparison to the mean orientation of  $S_{Hmax}$  derived from the WSM  
 274 (Heidbach et al., 2016) and additional data by Levi et al. (2019) are displayed in Figure 5. Figure 5a  
 275 shows the modelled  $S_{Hmax}$  orientation at 5000 m TVD (red lines) and the mean  $S_{Hmax}$  orientation (black  
 276 lines) with standard deviation (grey wedges) based on the WSM data. The angular deviation between  
 277 these two are displayed as a color plot (Figure 5b) and a histogram (Figure 5c). The mean orientation  
 278 of  $S_{Hmax}$  and standard deviation based on the WSM data is calculated using the stress2grid script of  
 279 Ziegler and Heidbach (2019b) that uses the statistics for circular data (Mardia, 1972). Input data

280 within a 200 km search radius are weighted by data quality and distance to a point of the  $0.5^\circ \times 0.5^\circ$   
281 grid (Ziegler and Heidbach, 2019a). Furthermore, at least 10 data records - with a quality of A to C -  
282 within the search radius must be available to return a mean  $S_{Hmax}$  orientation. In addition, data from  
283 the NGB within or above the Zechstein salt are sorted out to avoid effects due to salt decoupling  
284 (e.g., Roth and Fleckenstein, 2001; Röckel and Lempp, 2003 and Heidbach et al., 2007, since visco-  
285 elastic properties are not included in our model. For comparison, we use model results interpolated  
286 to 5000 m TVD.

287 As shown by Figure 5a, our model predicts an almost homogeneous N-S orientated stress pattern.  
288 The median deviation of  $0.3^\circ$  indicates an overall good fit to the mean WSM data. Furthermore,  
289 almost all results are within the standard deviation of the mean WSM data. However, Figure 5a and b  
290 indicate several model regions with significant deviations. For example, the local perturbations in the  
291 southern part of the model area where NNW-SSE orientations of  $S_{Hmax}$  dominate in the west and N-S  
292 orientations in the east or the NW-SE orientations in central Germany. In addition, the histogram  
293 (Figure 5c) shows an uneven distribution of the deviation.

294 3.2 Stress magnitudes and absolute stress state

295 3.2.1 Magnitudes of  $S_{hmin}$



296

297 Figure 6:  $S_{hmin}$  magnitudes of the model in comparison to data of Morawietz and Reiter (2020) used for calibration. (a)  
 298 Color-coded differences versus depth. Differences are calculated as model results minus calibration data. (b) Spatial  
 299 distribution of stress magnitude data, used for calibration. Numbers indicate localities with multiple data records. (c) Color-  
 300 coded histogram of the differences displayed in (a).

301 The magnitudes of  $S_{hmin}$  predicted by the model are displayed in comparison to calibration data by

302 Morawietz and Reiter, 2020. The differences are calculated as model results minus calibration data.

303 Thus, positive differences indicate too high values predicted by the model and negative differences

304 too low values. The differences in Figure 6a and Figure 6c are color-coded regarding their qualities.

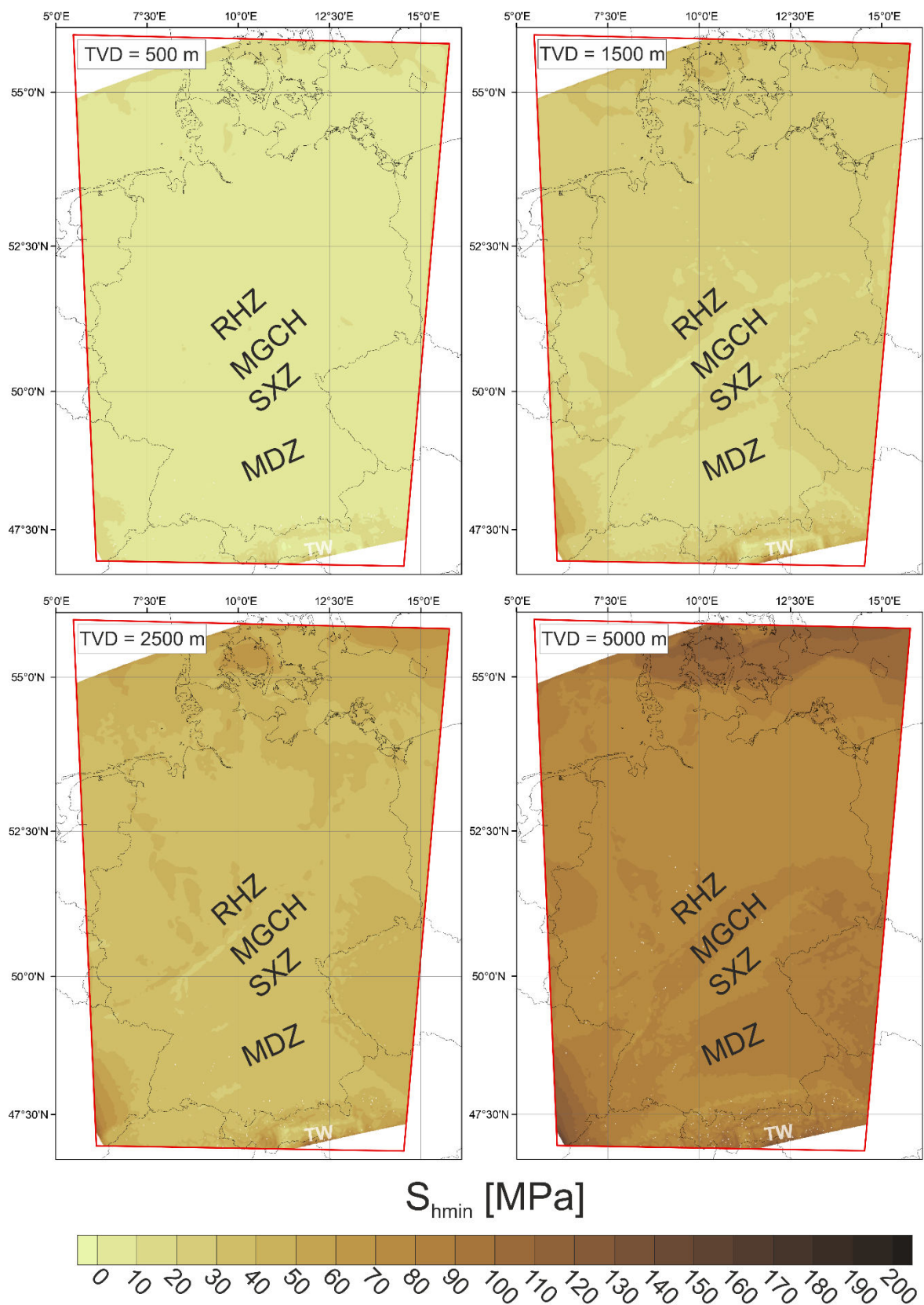
305 We use 73 values, from TVDs >200 m, with a quality of A to C from twelve localities mainly located in

306 south Germany with the exception of a data record from Peckensen (Röckel and Lempp, 2003). The  
307 localities are displayed in Figure 6b with numbers indicating multiple magnitudes from different  
308 depths at one location. In general, the fit regarding the  $S_{\text{hmin}}$  magnitudes of Morawietz and Reiter  
309 (2020) is good with differences in the range of -20 to 7.5 MPa and a mean of the absolute differences  
310 of 4.6 MPa. Figure 6a shows a depth trend from negative differences in the upper 1500 m indicating  
311 too low magnitudes predicted by the model to positive differences in greater depths indicating  
312 slightly too high magnitudes predicted. Due to the large amount of data in the upper 1000 m this  
313 leads to the unweighted median of -3.7 MPa and skewed histogram with a peak at -2.5 to -5 MPa.  
314 Therefore, we decided to use a depth-weighted median during the model calibration (chapter 2.7). A  
315 dependency on data qualities is not recognizable.

316 The depth sections displayed in Figure 7 show the  $S_{\text{hmin}}$  magnitudes at 500, 1500, 2500 and 5000 m  
317 TVD. The  $S_{\text{hmin}}$  at 500 m TVD shows a homogeneous stress distribution with values mainly between 0  
318 and 10 MPa. Only the northern and southern model edges show some larger magnitudes with the  
319 exception of the Tauern Window showing lower stresses equal to the main part of the model section.  
320 The section at 1500 m shows a less homogeneous stress distribution with dominant values between  
321 10 and 30 MPa. The highest values, up to 70 MPa in the southeast, are again, related to the model  
322 boundaries. The lowest values (0 to 10 MPa) occur along the border between the Rhenoherynian  
323 zone (RHZ) and the MGCH (Figure 1d) and in the western part of the Tauern Window. Striking are the  
324 lower values (10 to 20 MPa) within the area of the MDZ and the MGCH. Since, at 2500 m TVD these  
325 regions show the same magnitudes as the adjacent regions, in general, a homogeneous distribution  
326 with values between 30 and 40 MPa. The lowest values with 20 to 30 MPa again occur in the western  
327 part of the Tauern Window and at the border between RHZ and MGCH. The highest values are  
328 associated with the model edges. At 5000 m TVD, the stress distribution within the area of the MDZ  
329 and the MGCH seems to be inverted in comparison to the distribution at 1500 m TVD since the stress  
330 magnitudes are larger than in the adjacent areas e.g., the Saxothuringian zone (SXZ). In general, the

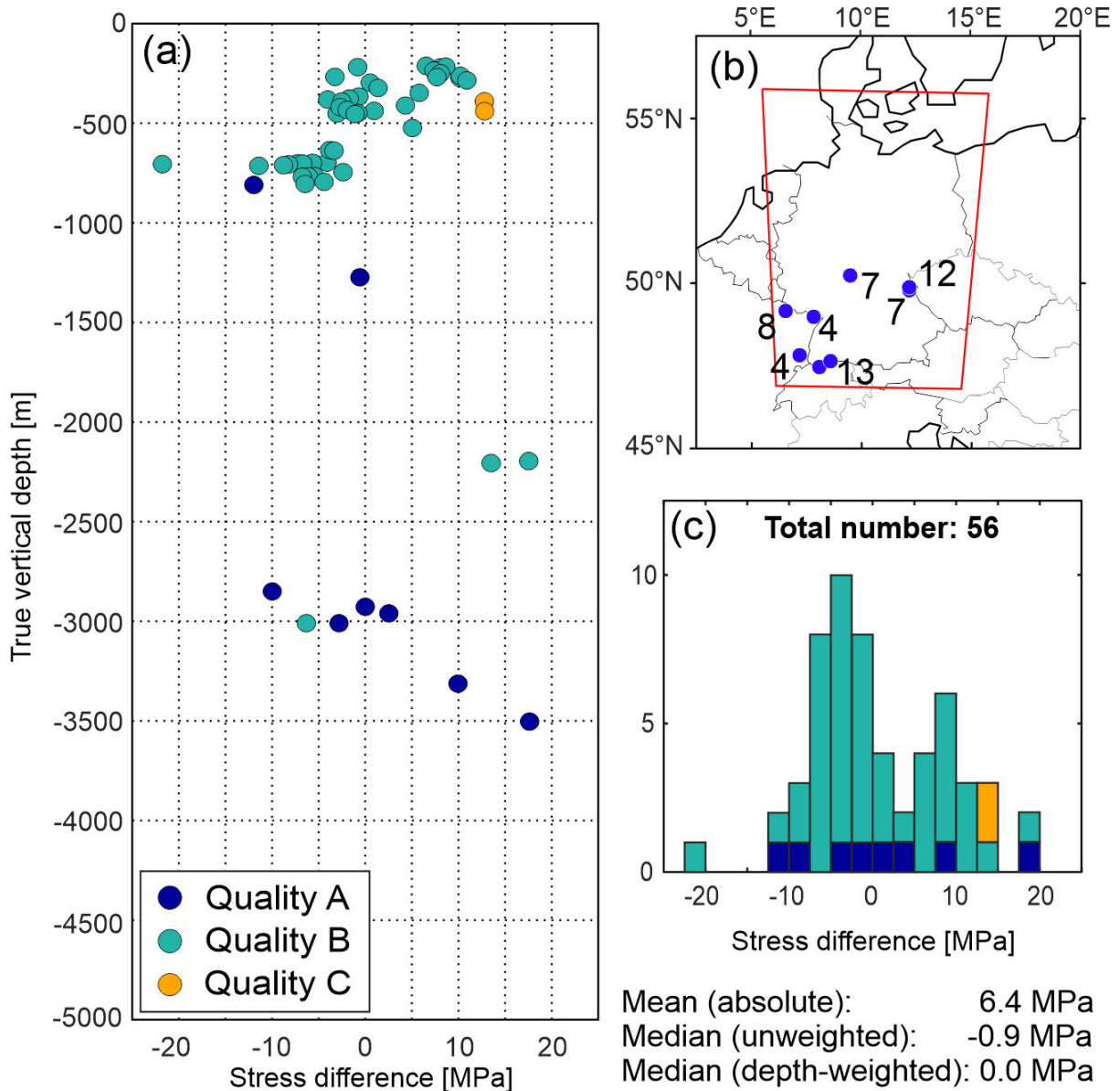
331 four depth sections of the model show a quite homogeneous distribution of  $S_{\text{hmin}}$  indicated by a  
332 maximum range of 20 to 30 MPa for each depth section, except for the model edges.

333



334

335 Figure 7: Depth sections showing the lateral distribution of the  $S_{hmin}$  magnitudes predicted by the model at four depth  
 336 sections by the model. TVD – true vertical depth. Black titles (details in Figure 1d): MDZ – Moldanubian Zone, MGCH – Mid  
 337 German Crystalline High, RHZ – Rhenoharzynian Zone, SXZ – Saxothuringian Zone. White title (details in Figure 1c): TW –  
 338 Tauern Window.

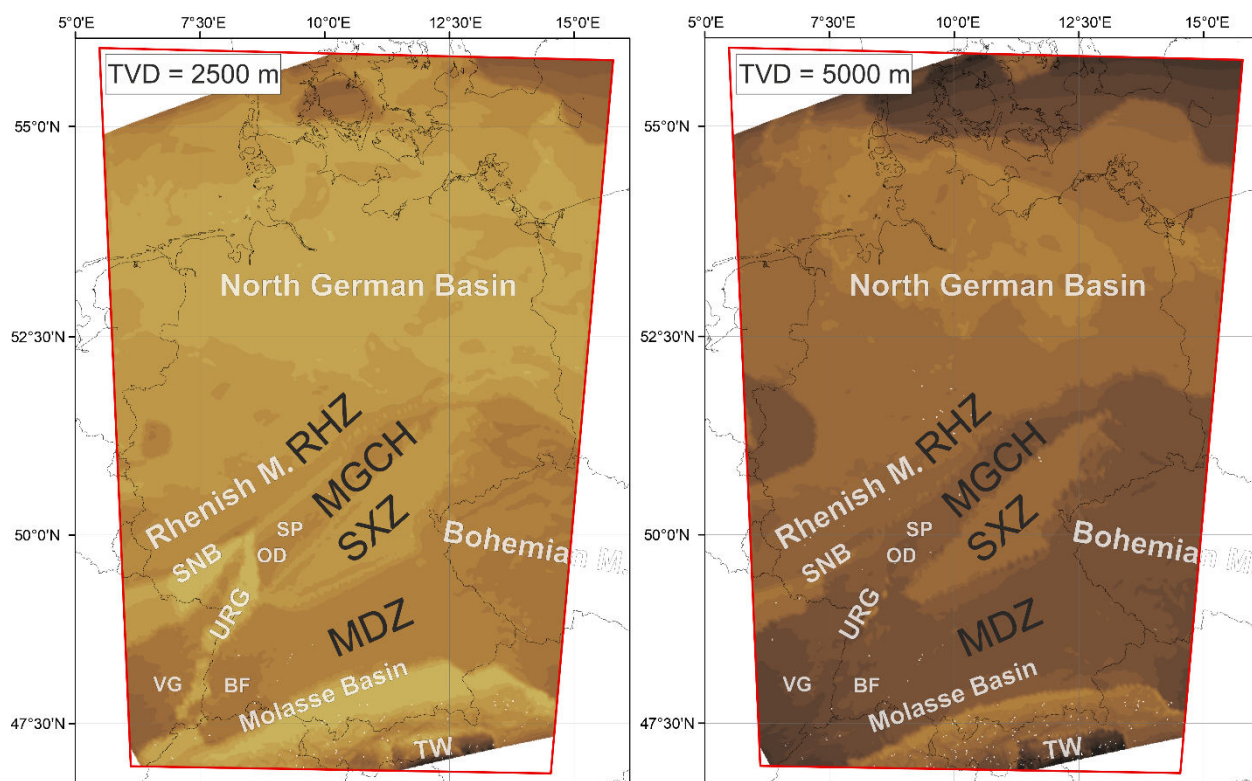
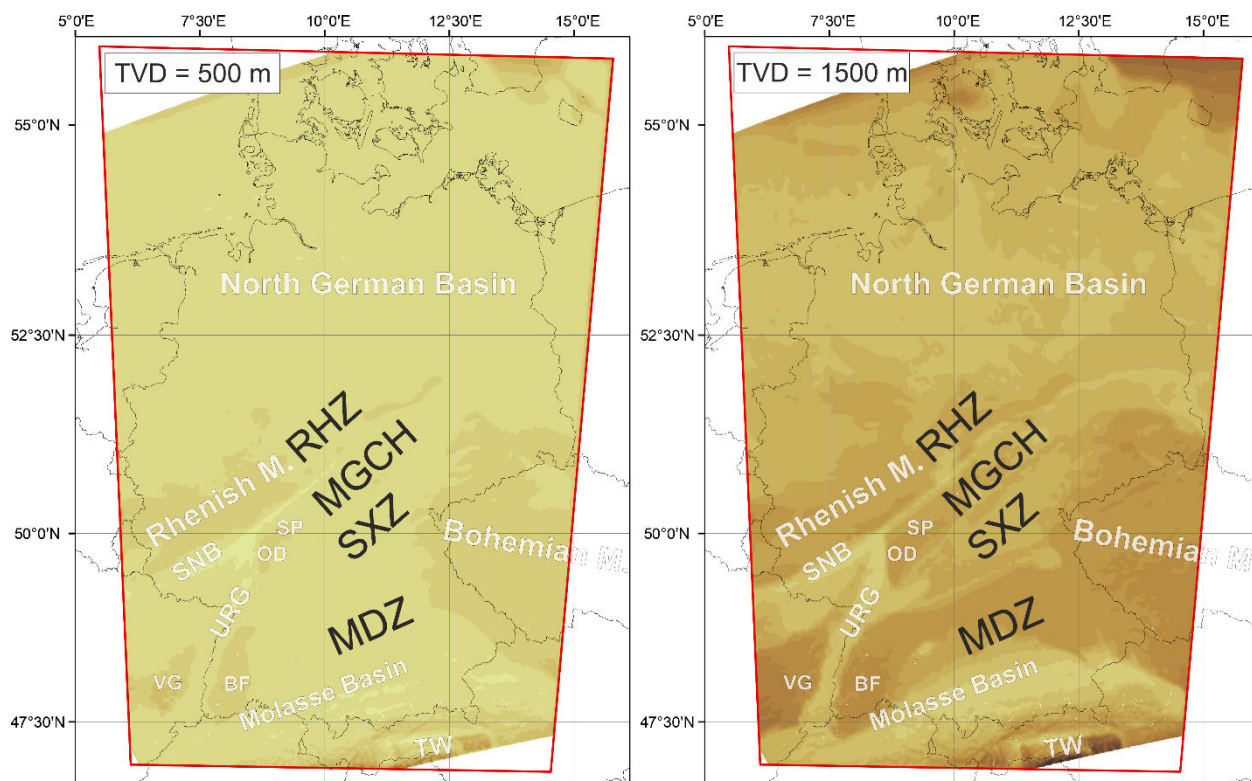


340

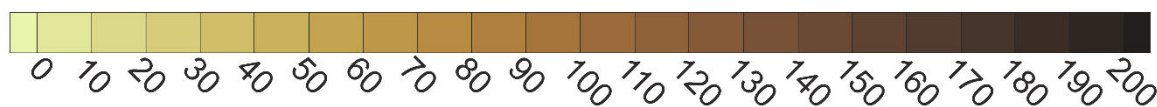
341 Figure 8:  $S_{Hmax}$  magnitudes of the model in comparison to data of Morawietz and Reiter (2020) used for calibration. (a)  
 342 Color-coded differences versus depth. Differences are calculated as model results minus calibration data. (b) Spatial  
 343 distribution of stress magnitude data, used for calibration. Numbers indicate localities with multiple data records. (c) Color-  
 344 coded histogram of the differences displayed in (a).

345 Figure 8 shows the  $S_{Hmax}$  magnitudes of the model in comparison to the calibration data of Morawietz  
 346 and Reiter (2020). Differences displayed in Figure 8a and Figure 8c are calculated as model results  
 347 minus calibration data. Thus, positive differences indicate too high values of  $S_{Hmax}$  predicted by the  
 348 model and negative differences too low  $S_{Hmax}$  magnitudes predicted. The differences are color-coded  
 349 depending on their qualities defined in the magnitude database by Morawietz et al. (2020). The  
 350 localities of the data used are displayed in Figure 8b. All data used, with a quality of A to C and from a

351 TVD >200 m are located at eight localities in southern Germany. The differences versus depth (Figure  
352 8a) and the histogram (Figure 8c) show a uniform distribution with a scattering of +/- 20 MPa. A  
353 dependency of depth or quality is not visible. The homogeneous fit between the model results and  
354 the calibration data is also indicated by the (unweighted) median of -0.9 MPa, which is almost equal  
355 to the depth-weighted median of 0.0 MPa. However, we also use the weighted median for the  
356 calibration with the  $S_{Hmax}$  magnitudes as for the  $S_{Hmin}$  magnitudes to use a constant calibration value.



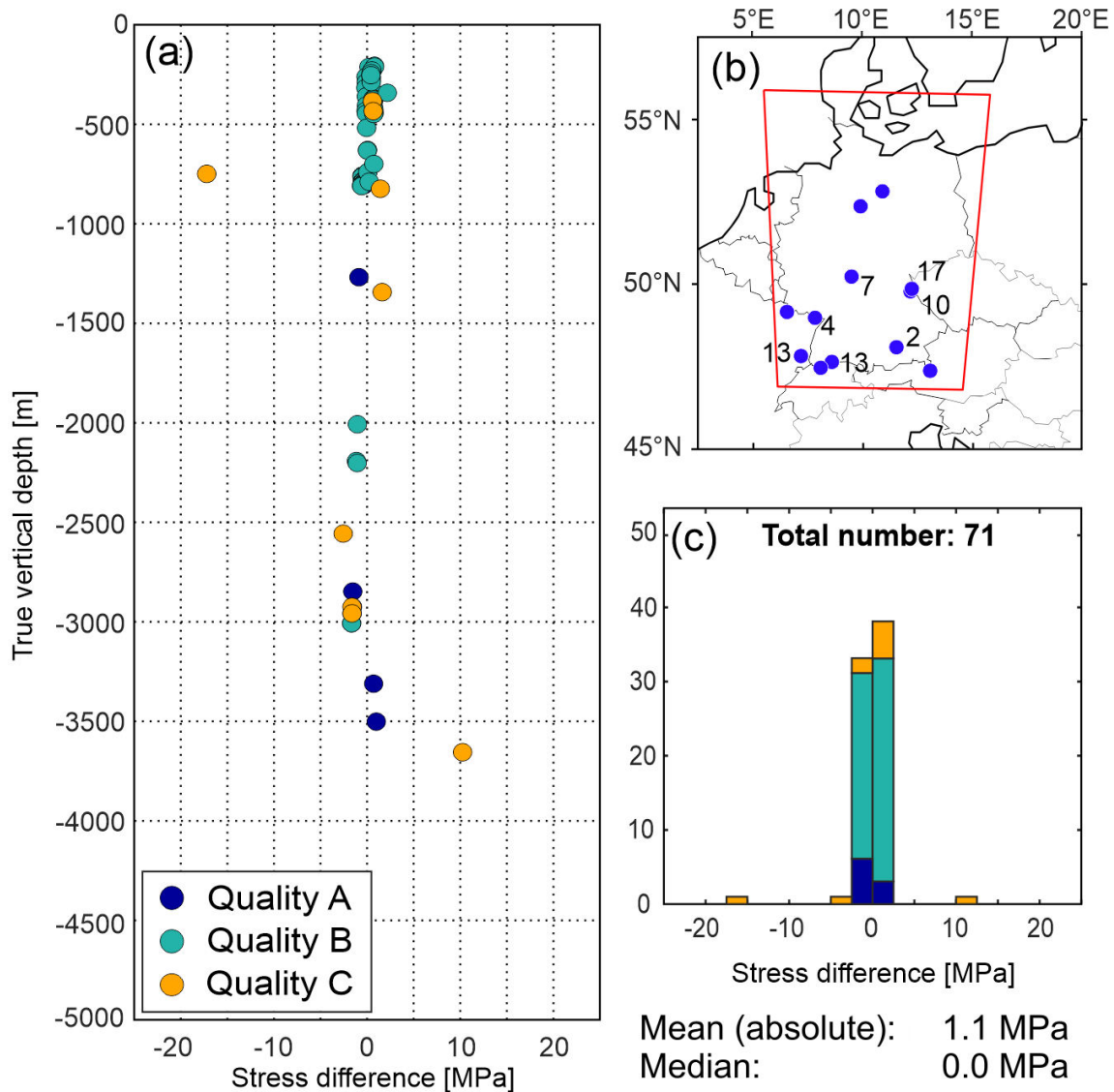
$S_{Hmax}$  [MPa]



358 Figure 9: Depth sections showing the lateral distribution of the  $S_{Hmax}$  magnitudes predicted by the model at four depth  
359 sections. TVD – true vertical depth. Black titles (details in Figure 1d): MDZ – Moldanubian Zone, MGCH – Mid German  
360 Crystalline High, RHZ – Rhenoharzynian Zone, SXZ – Saxothuringian Zone. White titles (details in Figure 1c): BF – Black  
361 Forest, M – Massif, OD – Odenwald, SNB – Saar-Nahe Basin, SP – Spessart, TW – Tauern Window, URG – Upper Rhine  
362 Graben, VG – Vosges.

363 To show the lateral distribution of the  $S_{Hmax}$  magnitudes four horizontal sections at 500, 1500, 2500  
364 and 5000 m TVD are displayed in Figure 9. At 500 m TVD, the magnitudes range from 0 to 30 MPa.  
365 The lowest magnitudes with 0 to 10 MPa are located within the MGCH in the vicinity to the RHZ and  
366 in the Tauern Window. The highest values of >20 MPa are associated with the model edges in the  
367 north and south and the basement outcrops of the southwestern Rhenish Massif, the Bohemian  
368 Massif, the Vosges, the Black Forest, the Odenwald and the Spessart. The section at 1500 m TVD  
369 shows a more differentiated distribution of  $S_{Hmax}$  with values ranging from 20 to 60 MPa, with some  
370 exception along the model edges. The higher values are again associated with outcropping basement  
371 structures like the Bohemian Massif. Regions with lower  $S_{Hmax}$  magnitudes between 20 and 40 MPa  
372 are located in the MB, the URG, the Saar-Nahe Basin (SNB), the NGB and the northern part of the  
373 MGCH in the vicinity of the RHZ. The results at 2500 and 5000 m TVD confirm the trend of higher  
374 magnitudes within the areas belonging to basement structures and lower magnitudes belonging to  
375 sedimentary units. An exception is the southwestern part of the Rhenish Massif, where the  
376 magnitudes do not increase as much as within the areas of crystalline basements. Finally, at 5000 m  
377 TVD the higher  $S_{Hmax}$  magnitudes correspond to areas with outcropping or shallow lying crystalline  
378 basement structures and lower  $S_{Hmax}$  magnitudes to sedimentary or low-grade metamorphic units.

379 3.2.3 Magnitudes of SV



380

381 Figure 10:  $S_v$  magnitudes of the model in comparison to data of Morawietz and Reiter (2020). (a) Color-coded differences  
 382 versus depth. Differences are calculated as model results minus data of Morawietz and Reiter (2020). (b) Spatial distribution  
 383 of stress magnitude data, used for calibration. Numbers indicate localities with multiple data. (c) Color-coded histogram of  
 384 the differences displayed in (a).

385 The differences between  $S_v$  magnitudes and the data by Morawietz and Reiter (2020) are displayed  
 386 in Figure 10. They are calculated as model results minus data of the magnitude database. Thus, too  
 387 high model results lead to positive differences, too low model results to negative differences. Since  
 388 the  $S_v$  magnitudes depend almost entirely on the density and are not influenced by displacement  
 389 boundary conditions applied, we did not use these data for calibration but for validation to check if  
 390 the densities chosen are reasonable. We use 71 values of Morawietz and Reiter (2020) from twelve  
 391 localities (Figure 10b). As the results show, the data used from the 3DD model (Anikiev et al., 2019)

392 are very appropriate. With the exception of two values at 750 and 3700 m TVD all differences are in  
 393 the range of -2.5 to 2.5 MPa, resulting in a mean of the absolute differences of 1.1 MPa and a median  
 394 of 0.0 MPa.

### 395 3.2.4 Regime Stress Ratio

396 To indicate the stress regime predicted by the model, the Regime Stress Ratio (RSR) for four model  
 397 sections at 500, 1500, 2500 and 5000 m TVD is shown in Figure 11. The RSR is a unitless value  
 398 between 0 and 3 describing seven stress states defined by Simpson (1997): radial extension (0), pure  
 399 normal faulting (0.5), transtension (1), pure strike-slip (1.5), transpression (2), pure reverse faulting  
 400 (2.5) and constriction (3). The RSR is derived from the regime index  $n$  (Anderson, 1905) and the ratio  
 401 of stress differences  $\phi$  (Angelier, 1979):

$$402 \quad RSR = (n + 0.5) + (-1)^n(\phi - 0.5) \quad (\text{Simpson, 1997}) \quad (3)$$

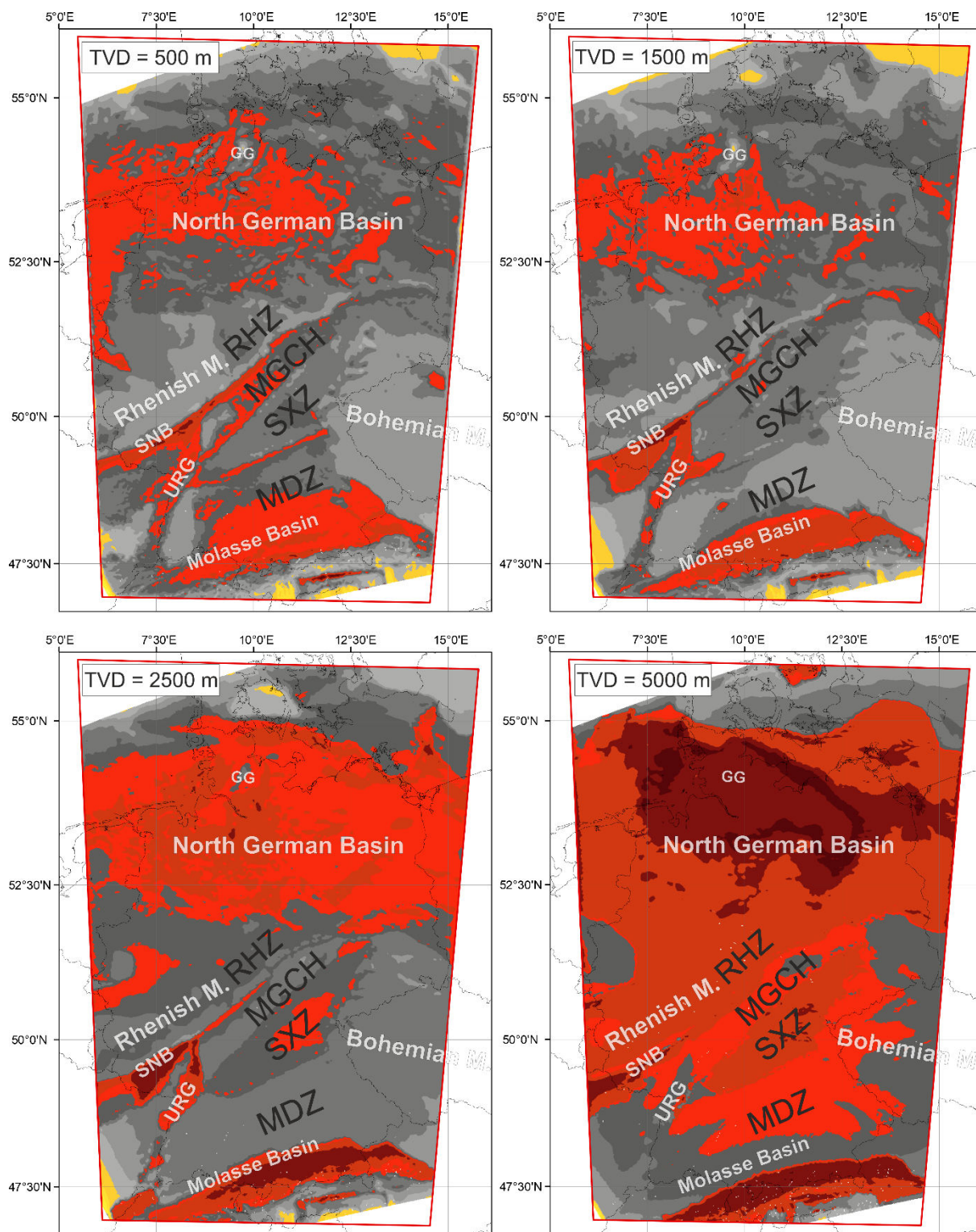
$$403 \quad n = \begin{cases} 0 & S_{hmin} < S_{Hmax} < S_V \\ 1 & S_{hmin} < S_V < S_{Hmax} \\ 2 & S_V < S_{hmin} < S_{Hmax} \end{cases} \quad (\text{Anderson, 1905}) \quad (4)$$

$$404 \quad \phi = \frac{(\sigma_2 - \sigma_3)}{(\sigma_1 - \sigma_3)} \quad (\text{Angelier, 1979}) \quad (5)$$

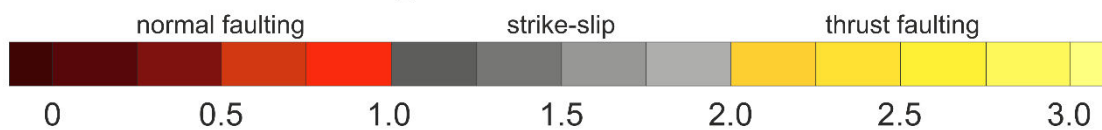
405 The calculated RSR values at 500 m TVD show a very inhomogeneous distribution, displaying the  
 406 whole range from thrust to normal faulting. Very high values - indicating a thrust faulting regime -  
 407 can be found e.g., at the model edges. Low values, indicating a normal faulting regime, occur e.g., in  
 408 the SNB, the URG, the NGB and in the MB. The model section at 1500 m TVD shows a more  
 409 homogeneous pattern than at 500 m TVD. RSR values larger than 2 occur still at the model edges and  
 410 within the area of the Glückstadt Graben. The lowest values still occur in the SNB, the URG, the NGB  
 411 and some areas within the MB. This trend continues at 2500 m TVD. Here, almost the entire SNB  
 412 show values  $< 0.5$  indicating a pure normal faulting regime. As at 1500 m TVD, also the NGB and the  
 413 southern part of the MB show a normal faulting regime and additionally also the SXZ. In contrast to  
 414 the 1500 m TVD section, several regions show lower values at 2500 m TVD. The deepest model  
 415 section shown at 5000 m TVD shows a much more homogeneous distribution than at 500 m with

416 large areas indicating a normal faulting regime. The trends described for 2500 m TVD continues,  
417 except within the URG. Up to a TVD of 2500 m the RSR in this area is lower in comparison to the  
418 surrounding areas, but at 5000 m TVD the RSR is higher.

419



## Regime Stress Ratio

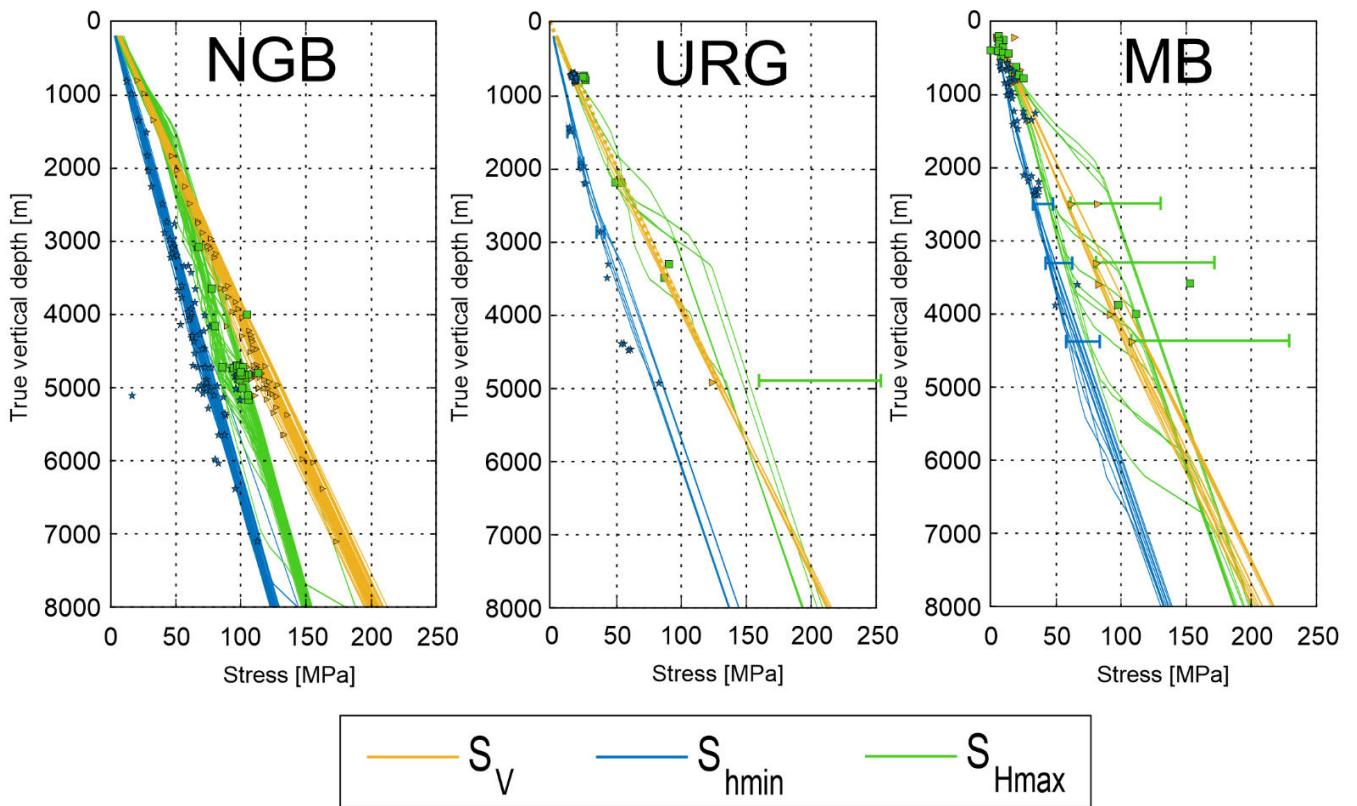


420

421 Figure 11: Four depth sections showing the lateral distribution of the Regime Stress Ratio (RSR) predicted by the model.  
 422 TVD – true vertical depth. Black titles (details in Figure 1d): MDZ – Moldanubian Zone, MGCH – Mid German Crystalline

423 High, RHZ – Rhenoharzynian Zone, SXZ – Saxothuringian Zone. White titles (details in Figure 1c): GG – Glückstadt Graben, M  
 424 – Massif, SNB – Saar-Nahe Basin, TW – Tauern Window, URG – Upper Rhine Graben.

425 3.2.5. Stress gradients



426

427 Figure 12: Results from multiple virtual wells in the corresponding sedimentary basin of the model in comparison to  
 428 measured and calculated magnitudes of  $S_V$ ,  $S_{hmin}$ , and  $S_{Hmax}$ . The uncertainties of the magnitudes if specified are displayed  
 429 as error bars. **North German Basin (NGB)**: Röckel and Lempp (2003), Fleckenstein et al. (2004), Stöckhert et al. (2013).  
 430 **Upper Rhine Graben (URG)**: Cornet and Burlet (1992), Klee and Rummel (1993), Valley and Evans (2007), Häring et al.  
 431 (2008), Meixner et al. (2014), Azzola et al. (2019). **Molasse Basin (MB)**: nagra (2001), Seithel et al. (2015), Backers et al.  
 432 (2017), Budach et al. (2017), Drews et al. (2019), Garrard et al. (2021).

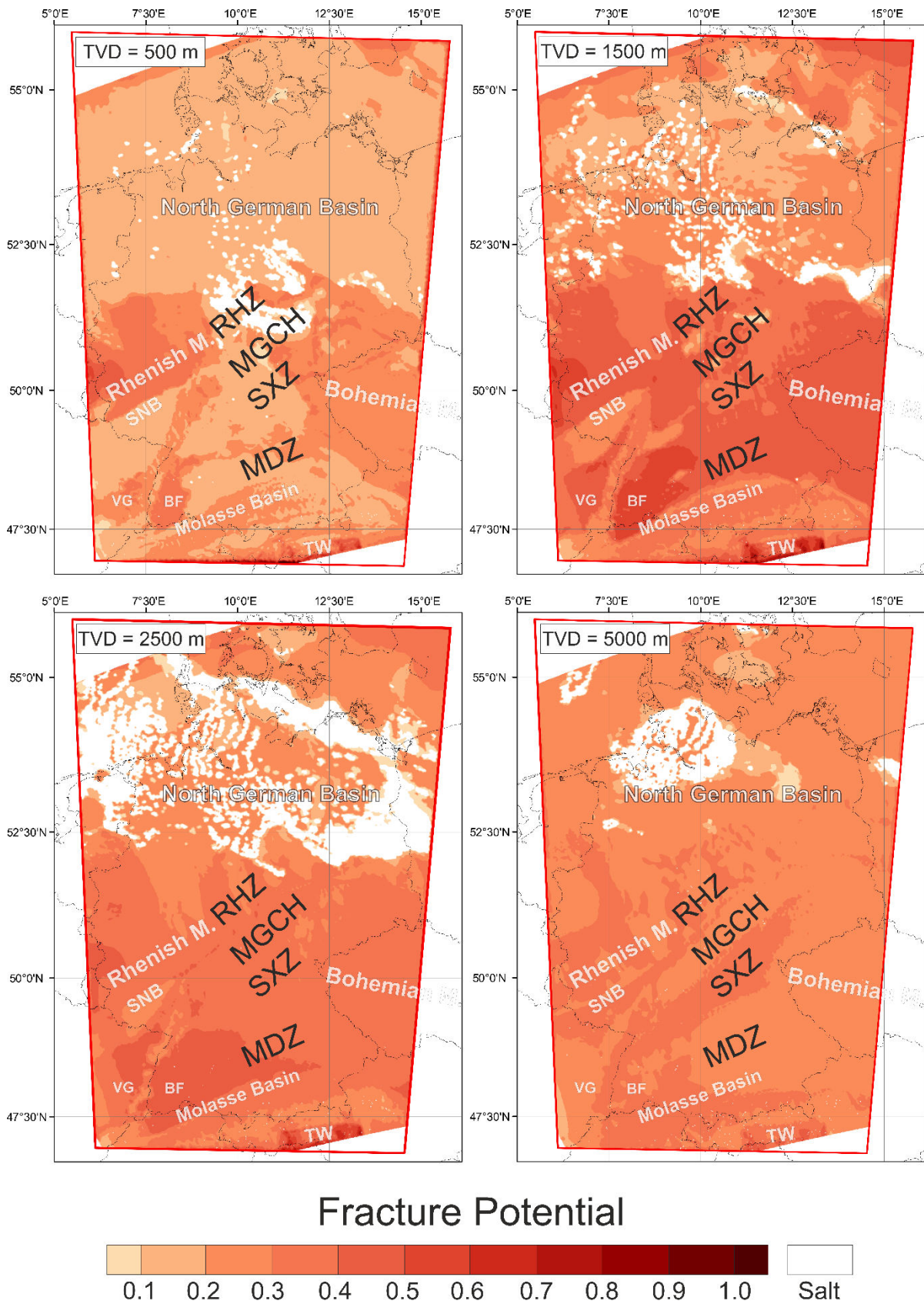
433 Figure 12 shows modeling results from three major sedimentary basins in Germany, the NGB, the  
 434 URG and the MB, in comparison to available data partially also used for calibration. Results and data  
 435 of the upper 200 m TVD are not displayed to avoid showing data influenced by topography or free  
 436 surface effects. The model results are displayed as magnitude sets ( $S_V$ ,  $S_{hmin}$  and  $S_{Hmax}$ ) from virtual  
 437 wells up to 8 km TVD located at the locations from which measurement data are shown. This results  
 438 in a compilation of 12 magnitude sets for the MB, five magnitude sets for the URG and 45 magnitude  
 439 sets for the NGB.

440 The results for the NGB show quite uniform magnitudes for all 45 magnitude sets displayed. The  
 441 modeled  $S_{hmin}$  magnitudes show the smallest range of values with a maximum range of  $\sim 10$  MPa

442 except for two outliers below ~5000 m TVD. The range of the  $S_{Hmax}$  magnitudes are larger with an  
443 average range of ~15 MPa, a maximum of ~25 MPa at ~5000 m TVD and again two outliers. The  $S_V$   
444 magnitudes show a trend of increasing scattering with depth, starting with a range of <5 MPa at 200  
445 m TVD to a range of ~20 MPa at 8 km TVD.

446 The five data sets from the URG show similar gradients for  $S_{hmin}$  and  $S_V$  but significant differences for  
447 the  $S_{Hmax}$  magnitudes. The  $S_{Hmax}$  magnitudes are also the only ones that show significant changes of  
448 the gradients with depth. While the  $S_{hmin}$  and  $S_V$  magnitudes show an almost linear increase with  
449 depth, some  $S_{Hmax}$  magnitudes between 2000 and 3500 m increase sharply and some even show  
450 decreasing or constant values. The compilation of the MB shows the most inhomogeneous results. At  
451 about 1000 m TVD, the magnitudes of  $S_{Hmax}$  split in two groups. The magnitudes of three virtual wells  
452 show an increase to ~40 MPa at 2500 m TVD in contrast to nine virtual wells, which show continuous  
453  $S_{Hmax}$  magnitudes. The  $S_V$  and  $S_{hmin}$  values of these three virtual wells also increase but less obviously  
454 to 5 to 10 MPa higher values. With increasing depth at about 2500, 3200, 3700, 4200, 5000 and 6000  
455 m TVD, other virtual wells also show such increasing magnitudes and converge to the higher  
456 magnitude trend. In general, there seems to be a lower and a higher magnitude gradient with a  
457 transition zone between 1000 and 6500 m TVD changing from one dominating gradient (0-1000 m  
458 TVD) to another (>6500 m TVD). At 8 km TVD, all magnitudes are roughly homogenous with  $S_{hmin}$   
459 magnitudes of 130 to 140 MPa,  $S_{Hmax}$  magnitudes of 180 to 200 MPa and  $S_V$  magnitudes of 200 to 215  
460 MPa.

461 3.2.6 Fracture Potential



462

463 Figure 13: Depth sections showing the lateral distribution of the Fracture Potential calculated for the model results. TVD –  
464 true vertical depth. Regions where Zechstein salt occurs are left white. Black titles (details in Figure 1d): MDZ –  
465 Moldanubian Zone, MGCH – Mid German Crystalline High, RHZ – Rhenoherynian Zone, SXZ – Saxothuringian Zone. White  
466 titles (details in Figure 1c): BF – Black Forest, M – Massif, SNB – Saar-Nahe Basin, TW – Tauern Window, VG – Vosges.

467 As an additional result the Fracture Potential (FP) of four depth sections is displayed in Figure 13. The  
468 FP based on Connolly and Cosgrove (1999) and Eckert and Connolly (2004) is a dimensionless value  
469 indicating how close to failure the stress state is. The calculation is described in detail by Heidbach et  
470 al. (2020). The FP is defined as *actual maximum shear stress* divided by the *acceptable shear stress*  
471 (Eq. 6):

$$472 \quad FP = \frac{\text{actual maximum shear stress}}{\text{acceptable shear stress}} \quad (6)$$

473 Therefore, a FP of >1 indicates failure and lower FPs represent a stable state of stress. The *actual*  
474 *maximum shear stress* is calculated as mean of the maximum ( $\sigma_1$ ) and minimum ( $\sigma_3$ ) principal stress  
475 (Eq. 7):

$$476 \quad \text{actual maximum shear stress} = \frac{1}{2}(\sigma_1 - \sigma_3) \quad (7)$$

477 The acceptable maximum shear stress is calculated as (Eq. 8):

$$478 \quad \text{acceptable shear stress} = C \cos\phi + \frac{1}{2}(\sigma_1 + \sigma_3) \sin\phi \quad (8)$$

479 The FP is calculated with individual cohesion (C) and friction angle ( $\phi$ ) for each model unit (Table 1),  
480 except for the Zechstein salt unit since salt behaves visco-elastic. Therefore, the regions where  
481 Zechstein salt occur are left white in Figure 13. The results in Figure 13 show a stable stress state  
482 with a FP between 0 and 0.6. The highest values of 0.5 to 0.6 occur at 1500 m depth. In general,  
483 there is an increase of the FP up to 1500 m TVD. With further increasing depth the FP decreases. At  
484 500 m TVD relative low values are associated with sedimentary units as within the NGB, the SNB or  
485 the Mesozoic units in southern Germany. Higher values are mainly associated with outcropping  
486 basement units, for example within the Bohemian and Rhenish Massif, the Vosges and the Black  
487 Forest. This trend is also visible at 1500 m TVD with a generally higher FP. High values are associated  
488 with crystalline basement units e.g., the MDZ, the MGCH or the Tauern Window, low values are

489 predicted for the NGB, the SNB or the MB. At 2500 m TVD such a clear trend is not visible anymore,  
490 but a low FP is still located within in the SNB. An interpretation of the results from the NGB is difficult  
491 for this depth section, since the Zechstein salt unit is dominant here. At 5000 m TVD the NGB is still a  
492 region with a relative low FP. However, in contrast to the depth sections at 500 or 1500 m TVD some  
493 regions show opposite trends. For example the Bohemian Massif with former relatively high values  
494 or the SNB with former relatively low values.

## 495 4 Discussion

### 496 4.1 Orientation of $S_{Hmax}$

497 Although our results lie almost entirely within the standard deviation of the  $S_{Hmax}$  orientation derived  
498 from the WSM and some additional data of Levi et al. (2019) and a median of deviation of  $0.3^\circ$   
499 suggest a very good fit, a closer look indicates some discrepancies (Figure 5). The orientations of  $S_{Hmax}$   
500 predicted by our model (Figure 5a) show a homogenous NNW-SSE pattern with some small deviation  
501 to N-S but the mean  $S_{Hmax}$  orientation of the WSM show several regions with divergent patterns e.g.,  
502 within the eastern part of the NGB showing NNE-SSW orientations or the central part of Germany  
503 with dominant NW-SE orientations. These results indicate that our model does probably not include  
504 some relevant factors or our displacement boundary conditions applied are too simple to reproduce  
505 the pattern of the orientation of  $S_{Hmax}$ . The median deviation of  $0.3^\circ$  and the distribution of the  
506 histogram support the former since differing displacements e.g., at the eastern and western edges  
507 would probably only shift the distribution as a whole. Implemented lateral stiffness contrasts do not  
508 seem to have a significant impact on the regional stress field e.g., predicted by Grünthal and  
509 Stromeyer (1994), Marotta et al. (2002) or Reiter (2021), despite Young's modulus contrasts of  $>50$   
510 GPa e.g., at the southern edge of the SNB between weak Rotliegend sediments (15 GPa) and the stiff  
511 upper crust (70 GPa). However, laterally there are no contrasts of the Young's modulus in the upper  
512 crystalline crust. Thus, the softer units lie on a homogeneous and stiff block. This could be an  
513 explanation of the quite homogeneous orientations of  $S_{Hmax}$ . Processes not included in our model,

514 which may also affect the stress field within the model region, are isostatic buoyancy effects in  
515 Scandinavia (Kaiser et al., 2005) or in the south due to erosion, deglaciation and potential slab break  
516 off below the Alpine chain (Przybycin et al., 2015; Sternai et al., 2019). In addition, the lithosphere-  
517 asthenosphere-boundary (Cacace, 2008) or density contrasts in the lower crust e.g., the Pritzwalk  
518 anomaly (Krawczyk et al., 2008) could explain the misfit in the northeast. Effects due to salt  
519 decoupling leading to a regional stress field below and a more local stress field above the Zechstein  
520 unit (Roth and Fleckenstein, 2001; Röckel and Lempp, 2003; Heidbach et al., 2007) should have no  
521 influence since we did not use the data from the units above.

## 522 4.2 Absolute stress and stress regime

523 In general, the predicted  $S_{hmin}$  magnitudes fit the values of Morawietz and Reiter (2020) quite well  
524 with differences between -20 and +7.5 MPa and a mean of the absolute differences of 4.6 MPa  
525 (Figure 6) and an overall good fit to additional data in Figure 12. However, the depth dependent  
526 differences (Figure 6a) and the compilation of the URG and the MB (Figure 12) indicate too low  
527 magnitudes of  $S_{hmin}$  within the upper ~1500 m of the model. Since the shallow calibration data  
528 (Figure 6b) and additional data of the MB (Figure 12) are partly located in young sedimentary units,  
529 the Young's modulus in the model could possibly be too high for these units, despite the  
530 implemented Young's modulus gradient. Furthermore, unconsolidated sediments can behave in a  
531 visco-elastic manner (e.g., Chang and Zoback, 1998, Zoback, 2007), which the linear elastic properties  
532 of our model cannot represent. Both, a lower Young's modulus and visco-elastic properties would  
533 lead to higher  $S_{hmin}$  magnitudes since the  $S_{hmin}$  magnitudes would approach the  $S_v$  magnitudes.  
534 Missing visco-elastic properties can also explain the too low values at ~800 m TVD, data from  
535 Wittelsheim, in the southwestern URG (Figure 12) measured in an evaporitic layer (Cornet and  
536 Burlet, 1992). Another clue to explain the low values could be the geographic distribution of the data.  
537 Almost all calibration data used and the data of the MB indicating this trend are located in the  
538 southern part of Germany. Available data from the northern part of Germany are sparse, but do not  
539 confirm this trend (Figure 12). A possible trend to slightly too high values in the lower part of the

540 model indicated by the three deepest values in the general comparison (Figure 6) cannot be  
541 confirmed by the results in Figure 12.

542 The predicted  $S_{Hmax}$  magnitudes also show a good fit to the values of the magnitude database by  
543 Morawietz and Reiter (2020) (Figure 8) despite a wider range of differences between -20 and +20  
544 MPa and a higher mean of the absolute differences of 6.4 MPa in comparison to the  $S_{hmin}$   
545 magnitudes. However, available  $S_{Hmax}$  magnitudes are usually calculated and not measured and  
546 therefore have larger uncertainties (Morawietz et al., 2020). Although the  $S_{Hmax}$  magnitudes of our  
547 model do not show a general depth trend as described for the  $S_{hmin}$  magnitudes, the differences in  
548 the upper 1000 m TVD show a distribution that is very similar to the one of the  $S_{hmin}$  magnitudes  
549 within this depth range (Figure 6 and Figure 8). This does not fit to the assumption that the Young's  
550 modulus might be too high because too low  $S_{Hmax}$  values rather indicate too low Young's modulus  
551 values. Incorporation of visco-elastic properties could increase both magnitudes if the  $S_{Hmax}$   
552 magnitudes are lower than  $S_v$ , which is partly the case indicated by a normal faulting regime in Figure  
553 11 and Figure 12. Another possibility to increase both horizontal magnitudes at the same time is an  
554 increase of the vertical stress, a higher Poisson's ratio, a higher stress input due to the boundary  
555 conditions or a higher k ratio of the initial stress. Increasing stresses by increasing the density does  
556 not seem to make sense since the fit with the  $S_v$  magnitudes (Figure 10) is almost perfect. A higher  
557 Poisson's ratio for different units within this specific depth interval only is difficult to explain. The  
558 third and fourth possibility, an increased shortening and reduced extension by the displacement  
559 boundary conditions or an increased k-ratio within the upper part of the model only, are difficult to  
560 implement and are difficult to explain from a tectonic point of view.

561 Another view inside the model is given by the compilation of virtual wells in Figure 12. The  
562 magnitudes used for comparison from the NGB are mainly based on two datasets. A compilation of  
563 Röckel and Lempp (2003) from the eastern and central part of the NGB and a dataset by Fleckenstein  
564 et al. (2004) from the western part of the NGB. The compilation of Röckel and Lempp (2003) only  
565 contains  $S_v$  and  $S_{hmin}$  magnitudes, the compilation of Fleckenstein et al. (2004) all three principal

566 stresses. However, the data sets show some general differences. The data from Fleckenstein et al.  
567 (2004) show a near isotropic stress state, particularly well visible between 4750 and 5250 m where  
568 the stress magnitudes of  $S_{hmin}$ ,  $S_{Hmax}$  and  $S_V$  are very close to each other. The smaller magnitudes of  
569  $S_{hmin}$  and also the larger  $S_V$  magnitudes visible within this depth range are from Röckel and Lempp  
570 (2003). In general, the model results of all virtual wells displayed show a better fit to the data of  
571 Röckel and Lempp (2003). However, it is remarkable that the  $S_{Hmax}$  magnitudes contrary to the  $S_{hmin}$   
572 and  $S_V$  magnitudes fit the data by Fleckenstein et al. (2004) quite well. The misfit between these  
573 datasets could be explained due to the different location within the NGB. Another possible reason for  
574 this discrepancy could be the different measurement methods, since the data by Fleckenstein et al.  
575 (2004) are based on core samples while the data of Röckel and Lempp (2003) are in-situ  
576 measurements. However, despite these inconsistencies the overall fit of the model results to the  
577 displayed data within the NGB is good.

578 The fit of the second virtual well compilation for the URG in comparison to the predicted magnitudes  
579 is also good. Regarding the  $S_{hmin}$  magnitudes, the results show only significant differences to the  
580 measured magnitudes at 800 m TVD and between 3500 and 4500 m TVD. The differences at ~800 m  
581 TVD, indicating ~10 MPa too low magnitudes, are probably a result of inappropriate material  
582 properties in the model for this area. As mentioned before, these dataset is measured in an  
583 evaporitic layer at Wittelsheim (Cornet and Burlet, 1992). However, our model does not include  
584 visco-elastic properties. Between 3500 and 4500 m TVD the model results indicate a trend to too  
585 high  $S_{hmin}$ . However, the deepest data record at 5000 m TVD fits to the model results. The  $S_{Hmax}$  data  
586 in general show a wider range of values as the  $S_{hmin}$  data. At ~800 and ~5000 m TVD our results  
587 indicate too low values. However, the value at 5000 m TVD from Basel (Häring et al., 2008) must be  
588 interpreted with care due to the very high uncertainty indicated by the error bar. The differences  
589 between 2000 and 3500 m TVD show significant deviations up to ~30 MPa but all data records are  
590 within the range of our predicted values. At ~2200 m TVD the lowest differences occur for all  
591 locations, except the results from Soultz-sous-Forets. Although both measured  $S_{Hmax}$  magnitudes

592 shown at 2200 m TVD are from Soultz-sous-Forets (Klee and Rummel, 1993) the model results from  
593 this region indicate too high values.. A possible explanation are altered granites in the upper part of  
594 the crystalline basement as described by Aichholzer et al. (2016) which are not well represented by  
595 our high Young's modulus of 70 GPa. A lower Young's modulus would possibly lead to lower  $S_{Hmax}$  and  
596 a better fit. However, the altered granites are only about 150 m thick and therefore not able to  
597 explain the full discrepancy. Remarkable are the  $S_{Hmax}$  magnitudes between 2500 and 3500 m TVD  
598 predicted for Bruchsal, showing a very low gradient leading to ~30 to 40 MPa lower values as  
599 predicted for the other locations. This trend can be explained by a thick Rotliegend layer within this  
600 region (GeORG-Projektteam, 2013; Meixner et al., 2014), with a low Young's modulus of 15 GPa. In  
601 addition, four of the five virtual wells show a significant change of the  $S_{Hmax}$  gradients with depth. For  
602 example, Rittershoffen and Soultz-sous-Forets - located only ~10 km apart from each other – show  
603 almost similar  $S_{Hmax}$  values below 3000 m TVD, but the gradient change occur below 1500 m TVD at  
604 Soultz-sous-Forets and below 2250 m TVD at Rittershoffen. The depth at which the 'jump' of the  
605  $S_{Hmax}$  magnitudes occurs fits quite perfectly to the boundary between the crystalline basement and  
606 the sedimentary units of the URG. Rittershoffen is a little east to Soultz-sous-Forets and further away  
607 from the western graben shoulder of the URG and therefore the top of the crystalline basement in  
608 Rittershoffen is located at ~2250 m TVD and at ~1550 m TVD in Soultz-sous-Forets (Aichholzer et al.,  
609 2016).

610 The  $S_{hmin}$  magnitudes of our model within the MB show a good fit to the comparison data displayed  
611 below 2000 m TVD. However, as already mentioned, our model results indicate partially too low  
612 values in the upper 1500 m. The  $S_{Hmax}$  magnitudes again show larger variations. Similar to the results  
613 of the URG, in all virtual wells the  $S_{Hmax}$  magnitudes increase if the crystalline basement is reached.  
614 Thus, since the depth of the crystalline basement differs in almost every virtual well due to the  
615 southward increase of the sediment thickness in the MB, the resulting stresses are inhomogeneous.  
616 A remarkable outlier is the data record at ~3600 m from Mauerstetten (Backers et al., 2017).

617 In general, the predicted  $S_{Hmax}$  magnitudes of the MB and URG show the impact of the vertical model  
618 resolution. The transition zone between sediments and crystalline basement is  $\sim 750$  m, which  
619 corresponds to about three element rows. A higher model resolution could decrease this transition  
620 zone significantly.

621 Since the calibration data (Figure 6 and Figure 8) and the compilations of Figure 12 only show  
622 pointwise data the  $S_{hmin}$  and  $S_{Hmax}$  magnitudes are additionally displayed by several depth sections to  
623 focus on the lateral distribution. In general, the depth sections of Figure 7 displaying the lateral  
624 distribution of the  $S_{hmin}$  magnitudes show a more homogeneous pattern than the  $S_{Hmax}$  magnitudes in  
625 Figure 9. However, in both figures high magnitudes of  $S_{hmin}$  or  $S_{Hmax}$  are associated with crystalline  
626 basement units e.g., the Bohemian Massif in the southeast or the EEC in the northeast and low  
627 magnitudes are often related to sedimentary basins e.g., the NGB or the MB or regions with  
628 outcropping low-grade metamorphic sediments e.g., the RHZ or SXZ. This correlation can be  
629 explained by the combination of stiff units with relatively high densities and softer units, which often  
630 have lower densities. However, a high stiffness alone is not sufficient for high horizontal stress  
631 magnitudes. This is because high stiffness leads to an increase in  $S_{Hmax}$  magnitudes as a result of  
632 applied shortening but at the same time to a decrease in the  $S_{hmin}$  magnitude as a result of applied  
633 extension. Accordingly, a higher Young's modulus leads to higher  $S_{Hmax}$  magnitudes and lower  $S_{hmin}$   
634 magnitudes. This effect can be reduced or increased by the influence of  $S_v$ .  $S_v$  reduces or increases  
635 the  $S_{hmin}$  and  $S_{Hmax}$  magnitudes equally and, since it is defined by density, a high density leads to  
636 higher horizontal stresses and a lower density to lower horizontal stresses. An example for this  
637 combined effect can be seen within the MDZ and MGCH where an inversion of the  $S_{hmin}$  magnitudes  
638 relative to the adjacent regions occurs between 1500 and 5000 m TVD (Figure 7). The MDZ and  
639 MGCH are regions with a thin sedimentary cover. Therefore, the low  $S_{hmin}$  magnitudes at 1500 m  
640 occur due to the high Young's modulus of 70 GPa and a lower magnitude of  $S_v$  due to the thin  
641 sedimentary cover. The adjacent regions show higher  $S_{hmin}$  magnitudes e.g., the Bohemian Massif  
642 with a similar Young's modulus but a higher  $S_v$  due to the missing sedimentary cover or the SXZ due

643 to a lower Young's modulus and a higher  $S_v$ . At 5000 m TVD the MDZ and MGCH show higher  $S_{hmin}$   
644 values than the SXZ but more similar to the ones in the Bohemian Massif. This shows that the effect  
645 of the thin sedimentary cover vanishes with depth. Furthermore, the relation between the  $S_{hmin}$   
646 magnitudes in the Bohemian Massif and the RHZ and NGB shows that the influence of a higher  
647 density (Bohemian Massif > RHZ & NGB) exceeds the effect of a lower Young's modulus (RHZ & NGB  
648 < Bohemian Massif). The lateral distribution of the  $S_{Hmax}$  magnitudes is easier to explain, since a  
649 higher density and a higher Young's modulus result in high stresses and a lower density and a lower  
650 Young's modulus in low stresses. Some boundary effects are visible at the northern and southern  
651 model edge where the compressional boundary conditions are defined, showing the highest values  
652 for  $S_{hmin}$  and  $S_{Hmax}$ . An exception is the stiff Tauern window (Young's modulus: 70 GPa), showing lower  
653 magnitudes of  $S_{hmin}$  and  $S_{Hmax}$  up to 1500 m TVD than the weaker surrounding thrust units of the  
654 Alps (Young's modulus: 23 GPa) do. This is probably due to the fact, that the Tauern window is  
655 pushed into the softer units and the soft units absorb the stress. This is also indicated by the high RSR  
656 values within the surrounding units (Figure 11, 500 to 2500 m TVD), indicating high horizontal  
657 stresses. Furthermore, remarkable low magnitudes of  $S_{hmin}$  and  $S_{Hmax}$  occur at the boundary between  
658 the RHZ and the MGCH up to 2500 m TVD. This might be an effect due to the vertical boundary  
659 between these units (Ahlers et al., 2021a).

660 The prediction of the stress regime and possible stress regime changes are important for the  
661 stimulation of geothermal reservoirs (Azzola et al., 2019), borehole stability and for directional  
662 drilling (Rajabi et al., 2016). In particular, if the stress regime change leads to an increase of the  
663 differential stress e.g., due to a change from a normal faulting to a strike-slip faulting regime. For  
664 this, the RSR indicating lateral and vertical stress regime changes is a useful parameter. For example  
665 the RSR values in the Glückstadt Graben up to 2500 m TVD, which are higher as in the adjacent areas  
666 of the NGB. Probably, the predicted strike-slip regime is related to major salt walls within this region  
667 (Maystrenko et al., 2005). The low density of salt ( $2100 \text{ kg/m}^3$ ) leads to a relative low  $S_v$  magnitude  
668 and, as a result, the horizontal stresses exceed  $S_v$  and even a thrust faulting regime at 1500 m TVD is

669 partially established. Very low RSR values at 2500 m TVD in the SNB show an opposite effect. The  
670 weak Rotliegend sediments with a Young's modulus of 15 GPa lead to low horizontal stresses and  
671 therefore the RSR value decreases, leading to a normal faulting regime. This is also well visible in the  
672 depth section at 5000 m TVD in the NGB. The trend towards relatively higher values in the URG than  
673 in the surrounding areas at 5 km TVD is related to a lower  $S_v$  in comparison to the graben shoulders  
674 because of the sedimentary fill of the URG but similar horizontal stresses. Above 5 km TVD, the  
675 horizontal stresses are lower in the URG due to the lower Young's modulus of the sediments.  
676 However, at 5 km TVD the basement of the URG is reached with a similar Young's modulus as for the  
677 graben shoulders. In general, a trend towards a normal faulting stress regime due to increasing  
678 dominance of  $S_v$  with depth is visible. Thus, the depth section at 5000 m TVD shows mainly RSR  
679 values smaller than 1.0.

680 This trend is also clearly visible in Figure 12. All results displayed show a stress regime change from a  
681 dominant strike-slip regime in the uppermost part of the model to a normal faulting regime at 8000  
682 m TVD. However, within the depth range of 200 to 8000 m TVD the results of the individual virtual  
683 wells differ sometimes significantly. The results from the NGB show an almost continuous change  
684 from a strike-slip regime in the upper 500 m to a normal faulting regime at TVDs >3000 m with a  
685 transition zone between 500 and 3000 m TVD where the stress regime is not the same for all virtual  
686 wells. The virtual wells located in the URG show a more complex stress regime change with depth,  
687 with differences up to 7500 m TVD. In the upper 1500 m, the magnitudes of  $S_v$  and  $S_{Hmax}$  are almost  
688 equal resulting in a strike-slip to reverse faulting regime or transpressional regime, respectively.  
689 Between 1500 and 2500 m TVD almost all  $S_{Hmax}$  magnitudes get higher than  $S_v$  resulting in a strike-  
690 slip regime. Between ~5500 and 7500 m TVD, the stress regime changes to a normal faulting regime.  
691 An exception are the results at Bruchsal, showing several changes of the stress regime up to 5500 m  
692 TVD between strike-slip and normal faulting regimes. The results of the MB show almost similar  
693 results as the results from the URG. Starting with a strike-slip to reverse faulting regime within the  
694 upper parts of the model, followed by a strike-slip regime and finally a normal faulting regime.

695

## 696 5 Conclusion

697 The model presented is a further step towards a robust prediction of the crustal stress state of  
698 Germany with focus on sedimentary basins. It is based on Ahlers et al. (2021a), but significantly  
699 improved. An eighteen-time higher mesh resolution resulting in a lateral resolution of 2.5 km and a  
700 vertical resolution of up to 250 m, 15 additional units within the sedimentary layer and an additional  
701 model calibration with  $S_{Hmax}$  magnitudes, provide a refined prediction of the crustal stress field of  
702 Germany. The 3D geomechanical-numerical model provides the complete 3D stress tensor for the  
703 entire model volume. Overall, the results show a good fit to all three principal stress magnitudes  $S_V$ ,  
704  $S_{hmin}$  and  $S_{Hmax}$  indicated by absolute differences of 0.0 MPa for  $S_V$ , 4.6 MPa for  $S_{hmin}$  and 6.4 MPa for  
705  $S_{Hmax}$ . The differences to the calibration data are mainly within in a range of +/- 10 MPa for the  $S_{hmin}$   
706 magnitudes and within a range of +/- 20 MPa for the  $S_{Hmax}$  magnitudes. Despite the overall good fit,  
707 some data indicate too low  $S_{hmin}$  values in the upper 1500 m TVD of our model. However, additional  
708 data from the NGB does not confirm a general trend. Apart from the magnitudes we compare our  
709 results also with a mean orientation of  $S_{Hmax}$  derived from the WSM (Heidbach et al., 2016) and  
710 additional data of Levi et al. (2019). Our predicted orientations of  $S_{Hmax}$  show an overall good fit with  
711 a median of 0.3° and our results lie almost entirely within the standard deviation of the derived WSM  
712 data. However, our model does not resolve perturbations of  $S_{Hmax}$  on smaller local scales as indicated  
713 by the data of the WSM.

714 Some limitations result from the size of our model. Due to the size, it is not possible to define  
715 visco-elastic properties e.g., for the Zechstein salt unit. Furthermore, the vertical resolution is still too  
716 low to numerically represent all units sufficiently and at the same time, some inhomogeneous units  
717 like the Triassic are still combined. Accordingly, sub modeling is a useful method to enable a higher  
718 resolution and stratigraphic refinement. Such smaller models enable also consideration of varying  
719 rock properties, a quantification of model uncertainties and the implementation of structures that

720 influence the stress field on a local scale e.g., faults. In addition, more high quality data records,  
721 especially magnitude data from north Germany are necessary for a more reliable calibration.

722 **List of abbreviations:**

723 3DD - 3D Deutschland  
724 ALCAPA - Alps-Carpathian-Pannonian  
725 ATA - Armorican Terrane Assemblage  
726 BF – Black Forest  
727 CG – Central Graben  
728 EEC - East European Craton  
729 EI – Eifel  
730 FP - Fracture Potential  
731 HG – Horn Graben  
732 HZ – Harz Mountains  
733 GG – Glückstadt Graben  
734 LRG – Lower Rhine Graben  
735 M- Massif  
736 MDZ – Moldanubian Zone  
737 MGCH – Mid German Crystalline High  
738 OD – Odenwald  
739 OG – Ohře Graben  
740 RHZ – Rhenoherynian Zone  
741 RSR – Regime Stress Ratio  
742  $S_{Hmax}$  – Maximum horizontal stress  
743  $S_{Hmin}$  – Minimum horizontal stress  
744 SNB – Saar-Nahe Basin  
745 SP – Spessart  
746  $S_v$  – Vertical stress  
747 SXZ – Saxothuringian Zone  
748 TVD – True vertical depth  
749 TW – Tauern Window  
750 URG – Upper Rhine Graben

751 VB – Vogelsberg Complex

752 VG – Vosges

753 WSM – World Stress Map

754

755 Declarations

756 **Availability of data and materials**

757 The model geometry and the results of our model have been published and are publicly available at:

758 <https://tudatalib.ulb.tu-darmstadt.de/handle/tudatalib/2624.5> (see Ahlers et al., 2021b).

759 **Competing interests**

760 'Not applicable'

761 **Funding**

762 This research has been supported by the Bundesministerium für Wirtschaft und Energie (grant

763 no. 02E11637A).

764 **Authors' contributions**

765 Conceptualization of the project was done by AH, TH, KR, OH and BM. Construction, discretization

766 and calibration of the model were done by SA. Data for the model and its calibration were collected

767 and provided by SA, LR, SM, MSW and DA. Evaluation of the model results and their interpretation

768 were performed by SA with the support of AH, TH, KR, BM, LR, OH and SM. SA wrote the paper with

769 help from all coauthors. All authors read and approved the final paper.

770 **Acknowledgements**

771 This study is part of the SpannEnD Project (<http://www.SpannEnD-Projekt.de>, last access:

772 2021/11/29), which is supported by Federal Ministry for Economic Affairs and Energy (BMWI) and

773 managed by Projektträger Karlsruhe (PTKA) (project code: 02E11637A). Calculations for this research  
774 were conducted on the Lichtenberg high performance computer of the Technische Universität  
775 Darmstadt. Coastlines and borders used in the figures are based on the Global Self-consistent  
776 Hierarchical High-resolution Geography (GSHHG) of Wessel and Smith (1996). We acknowledge  
777 support by the Deutsche Forschungsgemeinschaft (DFG – German Research Foundation) and the  
778 Open Access Publishing Fund of Technische Universität Darmstadt.

#### 779 **Authors' information (optional)**

780 'Not applicable'

#### 781 **References**

- 782 Ahlers, S., Henk, A., Hergert, T., Reiter, K., Müller, B., Röckel, L., Heidbach, O., Morawietz, S., Scheck-  
783 Wenderoth, M., and Anikiev, D.: 3D crustal stress state of Germany according to a data-calibrated  
784 geomechanical model, *Solid Earth*, 12, 1777–1799, <https://doi.org/10.5194/se-12-1777-2021>,  
785 2021a.
- 786 Ahlers, S., Henk, A., Hergert, T., Reiter, K., Müller, B., Röckel, L., Heidbach, O., Morawietz, S., Scheck-  
787 Wenderoth, M., and Anikiev, D.: The Crustal stress state of Germany - Results of a 3D  
788 geomechanical model v2, TUdataLib [data set], available at: [https://tudatalib.ulb.tu-](https://tudatalib.ulb.tu-darmstadt.de/handle/tudatalib/2624.5)  
789 [darmstadt.de/handle/tudatalib/2624.5](https://tudatalib.ulb.tu-darmstadt.de/handle/tudatalib/2624.5), 2021b.
- 790 Ahlers, S., Hergert, T., and Henk, A.: Numerical Modelling of Salt-Related Stress Decoupling in  
791 Sedimentary Basins–Motivated by Observational Data from the North German Basin,  
792 *Geosciences*, 9, <https://doi.org/10.3390/geosciences9010019>, 2019.
- 793 Aichholzer, C., Düringer, P., Orciani, S., and Genter, A.: New stratigraphic interpretation of the Soultz-  
794 sous-Forêts 30-year-old geothermal wells calibrated on the recent one from Rittershoffen (Upper  
795 Rhine Graben, France), *Geothermal Energy*, 4, 1–26, <https://doi.org/10.1186/s40517-016-0055-7>,  
796 2016.
- 797 Alber, M. and Solibida, C.: Geomechanical Characterization of a Host Rock for Enhanced Geothermal  
798 System in the North-German Basin, *Procedia Engineering*, 191, 158–163,  
799 <https://doi.org/10.1016/j.proeng.2017.05.167>, available at:  
800 <http://www.sciencedirect.com/science/article/pii/S187770581732307X>, 2017.
- 801 Alber, M., Backers, T., Bartmann, K., Brenne, S., Dinter, S., Dresen, G., Gipper, P., Gröhser, C., Heft, S.,  
802 Meier, T., Molenda, M., Röske, F., and Stöckhert, F.: Abschlussbericht zum  
803 Verbundprojekt: Erforschung der Mechanismen und Simulation hydraulisch induzierter Risse in  
804 geklüfteten Gesteinen für die Optimierung des Aufschlusses geothermischer Lagerstätten, Ruhr-  
805 Universität Bochum, geomecon GmbH, 2015.
- 806 Anderson, E. M.: The dynamics of faulting, *Transactions of the Edinburgh Geological Society*, 8, 387–  
807 402, <https://doi.org/10.1144/transed.8.3.387>, 1905.
- 808 Angelier, J.: Determination of the mean principal directions of stresses for a given fault population,  
809 *Tectonophysics*, 56, T17-T26, [https://doi.org/10.1016/0040-1951\(79\)90081-7](https://doi.org/10.1016/0040-1951(79)90081-7), 1979.

810 Anikiev, D., Lechel, A., Gomez Dacal, M. L., Bott, J., Cacace, M., and Scheck-Wenderoth, M.: A three-  
811 dimensional lithospheric-scale thermal model of Germany, *Adv. Geosci.*, 49, 225–234,  
812 <https://doi.org/10.5194/adgeo-49-225-2019>, 2019.

813 Asch, K.: The 1:5 Million International Geological Map of Europe and Adjacent Areas (IGME5000),  
814 Bundesanstalt für Geowissenschaften und Rohstoffe, Hannover, 2005.

815 Azzola, J., Valley, B., Schmittbuhl, J., and Genter, A.: Stress characterization and temporal evolution  
816 of borehole failure at the Rittershoffen geothermal project, *Solid Earth*, 10, 1155–1180,  
817 <https://doi.org/10.5194/se-10-1155-2019>, 2019.

818 Backers, T., Meier, T., Gipper, P., Munsch, P., Bücken, D., Nokar, K., Dinter, S., Grühser, C., Heft, S.,  
819 and Röske, F.: Abschlussbericht zum Teilprojekt B: Struktur- und Spannungsfeld im  
820 Verbundprojekt MAFA: Parametrisierung von Fazies, Diagenese, Struktur- und Spannungsfeld  
821 sowie Optimierung der Testabläufe im Malm zur Verringerung des Erfolgsrisikos, geomecon  
822 GmbH, 44 pp., 2017.

823 Bär, K., Reinsch, T., and Bott, J.: The PetroPhysical Property Database (P<sup>3</sup>) – a global compilation of  
824 lab-measured rock properties, *Earth Syst. Sci. Data*, 12, 2485–2515,  
825 <https://doi.org/10.5194/essd-12-2485-2020>, 2020.

826 Brückl, E., Behm, M., Decker, K., Grad, M., Guterch, A., Keller, G. R., and Thybo, H.: Crustal structure  
827 and active tectonics in the Eastern Alps, *Tectonics*, 29, TC2011,  
828 <https://doi.org/10.1029/2009TC002491>, 2010.

829 Buchmann, T. J. and Connolly, P. T.: Contemporary kinematics of the Upper Rhine Graben: A 3D finite  
830 element approach, *Global Planet. Change*, 58, 287–309,  
831 <https://doi.org/10.1016/j.gloplacha.2007.02.012>, 2007.

832 Budach, I., Moeck, I., Lüschen, E., and Wolfgramm, M.: Temporal evolution of fault systems in the  
833 Upper Jurassic of the Central German Molasse Basin: case study Unterhaching, *Geol Rundsch*,  
834 107, 635–653, <https://doi.org/10.1007/s00531-017-1518-1>, 2017.

835 Cacace, M.: Stress and Strain modelling of the Central European Basin System, Ph. D. thesis, Freie  
836 Universität Berlin, Berlin, 167 pp., 2008.

837 Cacace, M., Bayer, U., and Marotta, A. M.: Strain localization due to structural in-homogeneities in  
838 the Central European Basin System, *Geologische Rundschau*, 97, 899–913,  
839 <https://doi.org/10.1007/s00531-007-0192-0>, 2008.

840 Chang, C. T. and Zoback, M. D.: Viscous Rheology and State of Stress in Unconsolidated Sands, *Rock  
841 Mechanics in Petroleum Engineering*, Trondheim, Norway, July 1998., 465–473,  
842 <https://doi.org/10.2118/47401-MS>, 1998.

843 Connolly, P. and Cosgrove, J.: Prediction of static and dynamic fluid pathways within and around  
844 dilational jogs, *Geological Society, London, Special Publications*, 155, 105–121,  
845 <https://doi.org/10.1144/GSL.SP.1999.155.01.09>, 1999.

846 Cornet, F. H. and Burette, D.: Stress field determinations in France by hydraulic tests in boreholes, *J.  
847 Geophys. Res.-Sol. Ea.*, 97, 11829–11849, <https://doi.org/10.1029/90JB02638>, 1992.

848 Cornet, F. H. and Röckel, T.: Vertical stress profiles and the significance of “stress decoupling”,  
849 *Tectonophysics*, 581, 193–205, <https://doi.org/10.1016/j.tecto.2012.01.020>, available at:  
850 <http://www.sciencedirect.com/science/article/pii/S0040195112000480>, 2012.

851 Drews, M. C., Seithel, R., Savvatis, A., Kohl, T., and Stollhofen, H.: A normal-faulting stress regime in  
852 the Bavarian Foreland Molasse Basin? New evidence from detailed analysis of leak-off and  
853 formation integrity tests in the greater Munich area, SE-Germany, *Tectonophysics*, 755, 1–9,  
854 <https://doi.org/10.1016/j.tecto.2019.02.011>, 2019.

855 Dubelaar, C. W. and Nijland, T. G.: Early Cretaceous Obernkirchen and Bentheim Sandstones from  
856 Germany used as dimension stone in the Netherlands: geology, physical properties, architectural  
857 use and comparative weathering, in: *Geomaterials in construction and their sustainability:*

858 understanding their role in modern society, edited by: Přikryl, R., Török, Á., Theodoridou, M.,  
859 Gomez-Heras, M., and Miskovsky, K., 163–181, <https://doi.org/10.1144/SP416.13>, 2016.

860 Eckert, A. and Connolly, P.: 2D finite element modelling of regional and local fracture networks in the  
861 Eastern California shear zone and coso range, California USA, *Transactions - Geothermal*  
862 *Resources Council*, 28, 643–648, 2004.

863 Eynatten, H. von, Kley, J., Dunkl, I., Hoffmann, V.-E., and Simon, A.: Late Cretaceous to Paleogene  
864 exhumation in central Europe – localized inversion vs. large-scale domal uplift, *Solid Earth*, 12,  
865 935–958, <https://doi.org/10.5194/se-12-935-2021>, 2021.

866 Feist-Burkhardt, S., Götz, A. E., Szulc, J., Borkhataria, R., Geluk, M., Haas, J., Hornung, J., Jordan, P.,  
867 Kempf, O., Michalik, J., Nawrocki, J., Reinhardt, L., Ricken, W., Röhling, H.-G., Ruffer, T., Török, Á.,  
868 and Zühlke, R.: Triassic, in: *The Geology of Central Europe Volume 1: Precambrian and*  
869 *Palaeozoic; Volume 2: Mesozoic and Cenozoic*, edited by: McCann, T., The Geological Society of  
870 London, 749–821, <https://doi.org/10.1144/CEV2P.1>, 2008.

871 Fleckenstein, P., Reuschke, G., and Müller, B., and Connolly, P.: Predicting stress re-orientations  
872 associated with major geological structures in sedimentary sequences, *DGMK*, 593-5, 90 pp.,  
873 2004.

874 Garrard, R., Gonus, J., Desroches, J., and Bailey, E.: TBO Bülach-1-1: Data Report - Dossier IV Wireline  
875 Logging and Microhydraulic Fracturing, nagra, *Arbeitsbericht NAB*, 20-08, 2021.

876 GeORG-Projektteam: Geopotentiale des tieferen Untergrundes im Oberrheingraben: Fachlich-  
877 Technischer Abschlussbericht des INTERREG-Projekts GeORG, Teil 4, Freiburg i. Br., 104 pp., 2013.

878 Grünthal, G. and Stromeyer, D.: The recent crustal stress field in Central Europe sensu lato and its  
879 quantitative modelling, *Geologie en Mijnbouw*, 73, 173–180, 1994.

880 Häring, M. O., Schanz, U., Ladner, F., and Dyer, B. C.: Characterisation of the Basel 1 enhanced  
881 geothermal system, *Geothermics*, 37, 469–495,  
882 <https://doi.org/10.1016/j.geothermics.2008.06.002>, 2008.

883 Heidbach, O., Reinecker, J., Tingay, M., Müller, B., Sperner, B., Fuchs, K., and Wenzel, F.: Plate  
884 boundary forces are not enough: Second- and third-order stress patterns highlighted in the  
885 World Stress Map database, *Tectonics*, 26, TC6014, <https://doi.org/10.1029/2007TC002133>,  
886 2007.

887 Heidbach, O., Ziegler, M., and Stromeyer, D.: Manual of the Tecplot 360 Add-on GeoStress v2.0,  
888 World Stress Map Technical Report, 20-02, 62 pp., 2020.

889 Heidbach, O., Rajabi, M., Reiter, K., Ziegler, M., and WSM Team: World Stress Map Database Release  
890 2016 v1.1, GFZ Data Services [data set], <https://doi.org/10.5880/WSM.2016.001>, 2016.

891 Heidbach, O., Hergert, T., Reiter, K., and Giger, S.: NAB 13-88: Local Stress field sensitivity analysis -  
892 Case study Nördlich Langen, Wettingen, 50 pp., 2014.

893 Hergert, T., Heidbach, O., Reiter, K., Giger, S. B., and Marschall, P.: Stress field sensitivity analysis in a  
894 sedimentary sequence of the Alpine foreland, Northern Switzerland, *Solid Earth*, 6, 533–552,  
895 <https://doi.org/10.5194/se-6-533-2015>, 2015.

896 Hergert, T.: Numerical modelling of the absolute stress state in the Marmara region - a contribution  
897 to seismic hazard assessment, Dissertation, Universität Karlsruhe, 2009.

898 Hergert, T. and Heidbach, O.: Geomechanical model of the Marmara Sea region-II. 3-D contemporary  
899 background stress field, *Geophys. J. Int.*, 185, 1090–1102, [https://doi.org/10.1111/j.1365-](https://doi.org/10.1111/j.1365-246X.2011.04992.x)  
900 [246X.2011.04992.x](https://doi.org/10.1111/j.1365-246X.2011.04992.x), 2011.

901 Hudson, J. A. and Harrison, J. P.: Rock masses, in: *Engineering Rock Mechanics: An Introduction to the*  
902 *Principles*, edited by: Hudson, J. A. and Harrison, J. P., Elsevier, 141–148,  
903 <https://doi.org/10.1016/B978-008043864-1/50009-4>, 1997.

904 Ingebritsen, S. E. and Manning, C. E.: Geological implications of a permeability-depth curve for the  
905 continental crust, *Geol*, 27, 1107, [https://doi.org/10.1130/0091-](https://doi.org/10.1130/0091-7613(1999)027%3C1107:GIOAPD%3E2.3.CO;2)  
906 [7613\(1999\)027%3C1107:GIOAPD%3E2.3.CO;2](https://doi.org/10.1130/0091-7613(1999)027%3C1107:GIOAPD%3E2.3.CO;2), 1999.

907 Jarosiński, M., Beekman, F., Bada, G., and Cloetingh, S.: Redistribution of recent collision push and  
908 ridge push in Central Europe: insights from FEM modelling, *Geophys. J. Int.*, 167, 860–880,  
909 <https://doi.org/10.1111/j.1365-246X.2006.02979.x>, 2006.

910 Kaiser, A., Reicherter, K., Huebscher, C., Gajewski, D., Marotta, A. M., and Bayer, U.: Variation of the  
911 present-day stress field within the North German Basin; insights from thin shell FE modeling  
912 based on residual GPS velocities, *Tectonophysics*, 397, 55–72,  
913 <https://doi.org/10.1016/j.tecto.2004.10.009>, 2005.

914 Klee, G. and Rummel, F.: Hydrofrac stress data for the European HDR research project test site  
915 Soultz-Sous-Forêts, *Int. J. Rock Mech. Min*, 30, 973–976, [https://doi.org/10.1016/0148-](https://doi.org/10.1016/0148-9062(93)90054-H)  
916 [9062\(93\)90054-H](https://doi.org/10.1016/0148-9062(93)90054-H), 1993.

917 Kley, J., Franzke, H.-J., Jähne, F., Krawczyk, C., Lohr, T., Reicherter, K., Scheck-Wenderoth, M., Sippel,  
918 J., Tanner, D., and van Gent, H.: Strain and Stress, in: *Dynamics of complex intracontinental*  
919 *basins: The Central European basin system*, edited by: Littke, R., Bayer, U., Gajewski, D., and  
920 Nelskamp, S., Springer, Berlin, Heidelberg, 97–124, [https://doi.org/10.1007/978-3-540-85085-](https://doi.org/10.1007/978-3-540-85085-4_3)  
921 [4\\_3](https://doi.org/10.1007/978-3-540-85085-4_3), 2008.

922 Kley, J. and Voigt, T.: Late Cretaceous intraplate thrusting in central Europe: Effect of Africa-Iberia-  
923 Europe convergence, not Alpine collision, *Geology*, 36, 839–842,  
924 <https://doi.org/10.1130/G24930A.1>, 2008.

925 Krawczyk, C. M., Rabbel, W., Willert, S., Hese, F., Götze, H.-J., Gajewski, D., and SPP-Geophysics  
926 Group: Crustal structures and properties in the Central European Basin system from geophysical  
927 evidence, in: *Dynamics of complex intracontinental basins: The Central European basin system*,  
928 edited by: Littke, R., Bayer, U., Gajewski, D., and Nelskamp, S., Springer, Berlin, Heidelberg, 67–  
929 95, [https://doi.org/10.1007/978-3-540-85085-4\\_3](https://doi.org/10.1007/978-3-540-85085-4_3), 2008.

930 Kroner, U., Romer, R. L., and Linnemann, U.: The Saxo-Thuringian Zone of the Variscan Orogen as part  
931 of Pangea, in: *Pre-Mesozoic geology of Saxo-Thuringia: From the Cadomian active margin to the*  
932 *Variscan orogen*, edited by: Linnemann, U. and Romer, R. L., Schweizerbart, Stuttgart, 3–16,  
933 2010.

934 Levi, N., Habermueller, M., Exner, U., Piani, E., Wiesmayr, G., and Decker, K.: The stress field in the  
935 frontal part of the Eastern Alps (Austria) from borehole image log data, *Tectonophysics*, 769,  
936 228175, <https://doi.org/10.1016/j.tecto.2019.228175>, 2019.

937 Linnemann, U. and Romer, R. L. (Eds.): *Pre-Mesozoic geology of Saxo-Thuringia: From the Cadomian*  
938 *active margin to the Variscan orogen*, Schweizerbart, Stuttgart, 485 pp., 2010.

939 Litt, T., Schmincke, H.-U., Frechen, M., and Schluchter, C.: Quaternary, in: *The Geology of Central*  
940 *Europe Volume 1: Precambrian and Palaeozoic; Volume 2: Mesozoic and Cenozoic*, edited by:  
941 McCann, T., The Geological Society of London, 1287–1340, <https://doi.org/10.1144/CEV2P.8>,  
942 2008.

943 Mardia, K. V.: *Statistics of Directional Data: Probability and Mathematical Statistics*, Academic Press,  
944 London, 380 pp., 1972.

945 Marotta, A. M., Bayer, U., Thybo, H., and Scheck, M.: Origin of the regional stress in the North  
946 German Basin - results from numerical modelling, *Tectonophysics*, 360, 245–264,  
947 [https://doi.org/10.1016/S0040-1951\(02\)00358-X](https://doi.org/10.1016/S0040-1951(02)00358-X), 2002.

948 Maystrenko, Y., Bayer, U., and Scheck-Wenderoth, M.: The Glueckstadt Graben, a sedimentary  
949 record between the North and Baltic Sea in north Central Europe, *Tectonophysics*, 397, 113–126,  
950 <https://doi.org/10.1016/j.tecto.2004.10.004>, available at:  
951 <https://www.sciencedirect.com/science/article/pii/S0040195104004482>, 2005.

952 Maystrenko, Y. P. and Scheck-Wenderoth, M.: 3D lithosphere-scale density model of the Central  
953 European Basin System and adjacent areas, *Tectonophysics*, 601, 53–77,  
954 <https://doi.org/10.1016/j.tecto.2013.04.023>, 2013.

955 McCann, T. (Ed.): *The Geology of Central Europe Volume 1: Precambrian and Palaeozoic; Volume 2:*  
956 *Mesozoic and Cenozoic*, The Geological Society of London, 1449 pp., 2008.

957 McCann, T., Kiersnowski, H., Krainer, K., Vozarova, A., Peryt, T. M., Oplustil, S., Stollhofen, H.,  
958 Schneider, J., Wetzel, A., Boulvain, F., Duser, M., Torok, A., Haas, J., Tait, J., and Korner, F.:  
959 Permian, in: *The Geology of Central Europe Volume 1: Precambrian and Palaeozoic; Volume 2:*  
960 *Mesozoic and Cenozoic*, edited by: McCann, T., The Geological Society of London, 531–597,  
961 <https://doi.org/10.1144/CEV1P.10>, 2008.

962 Meixner, J., Schill, E., Gaucher, E., and Kohl, T.: Inferring the in situ stress regime in deep sediments:  
963 an example from the Bruchsal geothermal site, *Geotherm Energy*, 2,  
964 <https://doi.org/10.1186/s40517-014-0007-z>, 2014.

965 Morawietz, S. and Reiter, K.: Stress Magnitude Database Germany v1.0, GFZ Data Services [data set],  
966 <https://doi.org/10.5880/wsm.2020.004>, 2020.

967 Morawietz, S., Heidbach, O., Reiter, K., Ziegler, M., Rajabi, M., Zimmermann, G., Müller, B., and  
968 Tingay, M.: An open-access stress magnitude database for Germany and adjacent regions,  
969 *Geothermal Energy*, 8, <https://doi.org/10.1186/s40517-020-00178-5>, 2020.

970 nagra: Sondierbohrung Benken: Technical Report NTB 00-01, nagra, 288 pp., 2001.

971 Pienkowski, G., Schudack, M. E., Bosak, P., Enay, R., Feldman-Olszewska, A., Golonka, J., Gutowski, J.,  
972 Hengreen, G., Jordan, P., Krobicki, M., Lathuiliere, B., Leinfelder, R. R., Michalik, J., Monnig, E.,  
973 Noe-Nygaard, N., Palfy, J., Pint, A., Rasser, M. W., Reisdorf, A. G., Schmid, D. U., Schweigert, G.,  
974 Surlyk, F., Wetzel, A., and Wong, T. E.: Jurassic, in: *The Geology of Central Europe Volume 1:*  
975 *Precambrian and Palaeozoic; Volume 2: Mesozoic and Cenozoic*, edited by: McCann, T., The  
976 Geological Society of London, 823–922, <https://doi.org/10.1144/CEV2P.2>, 2008.

977 Przybycin, A. M., Scheck-Wenderoth, M., and Schneider, M.: Assessment of the isostatic state and  
978 the load distribution of the European Molasse Basin by means of lithospheric scale 3D structural  
979 and 3D gravity modelling, *Int. J. Earth Sci.*, 104, 1405–1424, [https://doi.org/10.1007/s00531-014-](https://doi.org/10.1007/s00531-014-1132-4)  
980 1132-4, 2015.

981 Rajabi, M., Tingay, M., and Heidbach, O.: The present-day state of tectonic stress in the Darling Basin,  
982 Australia: Implications for exploration and production, *Mar. Petrol. Geol.*, 77, 776–790,  
983 <https://doi.org/10.1016/j.marpetgeo.2016.07.021>, 2016.

984 Rasser, M. W., Harzhauser, M., Anistratenko, O. Y., Anistratenko, V. V., Bassi, D., Belak, M., Berger, J.-  
985 P., Bianchini, G., Cicic, S., Cosovic, V., Dolakova, N., Drobne, K., Filipescu, S., Gürs, K., Hladilova, S.,  
986 Hrvatovic, H., Jelen, B., Kasinski, J. R., Kovac, M., Kralj, P., Marjanac, T., Marton, E., Mietto, P.,  
987 Moro, A., Nagymarosy, A., Nebelsick, J. H., Nehyba, S., Ogorelec, B., Oszypko, N., Pavelic, D.,  
988 Pavlovec, R., Pavsic, J., Petrova, P., Piwocki, M., Poljak, M., Pugliese, N., Redzepovic, R., Rifelj, H.,  
989 Roetzel, R., Skaberne, D., Sliva, L., Standke, G., Tunis, G., Vass, D., Wagreeich, M., and Wesselingh,  
990 F.: Palaeogene and Neogene, in: *The Geology of Central Europe Volume 1: Precambrian and*  
991 *Palaeozoic; Volume 2: Mesozoic and Cenozoic*, edited by: McCann, T., The Geological Society of  
992 London, 1031–1139, <https://doi.org/10.1144/CEV2P.5>, 2008.

993 Reicherter, K., Froitzheim, N., Jarosinski, M., Badura, J., Franzke, H.-J., Hansen, M., Hubscher, C.,  
994 Müller, R., Poprawa, P., Reinecker, J., Stackebrandt, W., Voigt, T., Eynatten, H. von, and  
995 Zuchiewicz, W.: Alpine tectonics north of the Alps, in: *The Geology of Central Europe Volume 1:*  
996 *Precambrian and Palaeozoic; Volume 2: Mesozoic and Cenozoic*, edited by: McCann, T., The  
997 Geological Society of London, 1233–1285, <https://doi.org/10.1144/CEV2P.7>, 2008.

998 Reiter, K. and Heidbach, O.: 3-D geomechanical–numerical model of the contemporary crustal stress  
999 state in the Alberta Basin (Canada), *Solid Earth*, 5, 1123–1149, [https://doi.org/10.5194/se-5-](https://doi.org/10.5194/se-5-1123-2014)  
1000 1123-2014, 2014.

1001 Reiter, K.: Stress rotation – impact and interaction of rock stiffness and faults, *Solid Earth*, 12, 1287–  
1002 1307, <https://doi.org/10.5194/se-12-1287-2021>, 2021.

1003 Reyer, D.: Outcrop analogue studies of rocks from the Northwest German Basin for geothermal  
1004 exploration and exploitation: Fault zone structure, heterogeneous rock properties, and  
1005 application to reservoir conditions, PhD, 108 pp., 2013.

1006 Röckel, T. and Lempp, C.: Der Spannungszustand im Norddeutschen Becken, *Erdöl-Erdgas-Kohle*, 119,  
1007 73–80, 2003.

1008 Roth, F. and Fleckenstein, P.: Stress orientations found in NE Germany differ from the West European  
1009 trend, *Terra Nova*, 13, 289–296, <https://doi.org/10.1046/j.1365-3121.2001.00357.x>, 2001.

1010 Scheck-Wenderoth, M. and Lamarche, J.: Crustal memory and basin evolution in the Central  
1011 European Basin System - new insights from a 3D structural model, *Tectonophysics*, 397, 143–165,  
1012 <https://doi.org/10.1016/j.tecto.2004.10.007>, 2005.

1013 Scheck-Wenderoth, M., Krzywiec, P., Zuhlke, R., Maystrenko, Y., and Froitzheim, N.: Permian to  
1014 Cretaceous tectonics, in: *The Geology of Central Europe Volume 1: Precambrian and Palaeozoic;*  
1015 *Volume 2: Mesozoic and Cenozoic*, edited by: McCann, T., The Geological Society of London, 999–  
1016 1030, <https://doi.org/10.1144/CEV2P.4>, 2008.

1017 Seithel, R., Steiner, U., Müller, B., Hecht, C., and Kohl, T.: Local stress anomaly in the Bavarian  
1018 Molasse Basin, *Geotherm Energy*, 3, <https://doi.org/10.1186/s40517-014-0023-z>, 2015.

1019 Sheorey, P. R.: A theory for In Situ stresses in isotropic and transverseley isotropic rock, *Int. J. Rock*  
1020 *Mech. Min*, 31, 23–34, [https://doi.org/10.1016/0148-9062\(94\)92312-4](https://doi.org/10.1016/0148-9062(94)92312-4), 1994.

1021 Simpson, R. W.: Quantifying Anderson's fault types, *J. Geophys. Res.*, 102, 17909–17919,  
1022 <https://doi.org/10.1029/97JB01274>, 1997.

1023 Sternai, P., Sue, C., Husson, L., Serpelloni, E., Becker, T. W., Willett, S. D., Faccenna, C., Di Giulio, A.,  
1024 Spada, G., Jolivet, L., Valla, P., Petit, C., Nocquet, J.-M., Walpersdorf, A., and Castelltort, S.:  
1025 Present-day uplift of the European Alps: Evaluating mechanisms and models of their relative  
1026 contributions, *Earth-Science Reviews*, 190, 589–604,  
1027 <https://doi.org/10.1016/j.earscirev.2019.01.005>, 2019.

1028 Stöckhert, F., Brenne, S., Molenda, M., Bartmann, K., Hoenig, S., and Alber, M.: Geomechanische  
1029 Charakterisierung von Vulkaniten und Sedimenten des Rotliegenden im Norddeutschen Becken  
1030 für die Optimierung des Aufschlusses geothermischer Lagerstätten, 19. Tagung für  
1031 Ingenieurgeologie mit Forum für junge Ingenieurgeologen, München 2013, 2013.

1032 Stollhofen, H., Bachmann, G., Barnasch, J., Bayer, U., Beutler, G., Franz, M., Kästner, M., Legler, B.,  
1033 Mutterlose, J., and Radies, D.: Basin Fill - Upper Rotliegend to Early Cretaceous basin  
1034 development, in: *Dynamics of complex intracontinental basins: The Central European basin*  
1035 *system*, edited by: Littke, R., Bayer, U., Gajewski, D., and Nelskamp, S., Springer, Berlin,  
1036 Heidelberg, 181–210, [https://doi.org/10.1007/978-3-540-85085-4\\_4](https://doi.org/10.1007/978-3-540-85085-4_4), 2008.

1037 Stromeyer, D. and Heidbach, O.: Tecplot 360 Add-on GeoStress, GFZ Data Services, 2017.

1038 Tašárová, Z. A., Fullea, J., Bielik, M., and Šroda, P.: Lithospheric structure of Central Europe: Puzzle  
1039 pieces from Pannonian Basin to Trans-European Suture Zone resolved by geophysical-petrological  
1040 modeling, *Tectonics*, 35, 722–753, <https://doi.org/10.1002/2015TC003935>, 2016.

1041 Turcotte, D. L. and Schubert, G.: *Geodynamics*, 3. ed., Cambridge Univ. Press, Cambridge, 623 pp.,  
1042 2014.

1043 Urai, J. L., Schlöder, Z., Spiers, C. K., and Kukla, P. A.: Flow and Transport Properties of Salt Rocks, in:  
1044 *Dynamics of complex intracontinental basins: The Central European basin system*, edited by:  
1045 Littke, R., Bayer, U., Gajewski, D., and Nelskamp, S., Springer, Berlin, Heidelberg, 277–290, 2008.

1046 Valley, B. and Evans, K. F.: Stress State at Soultz-Sous-Forêts to 5 km Depth from wellbore failure and  
1047 hydraulic observations, in: Thirty-Second Workshop on Geothermal Reservoir Engineering, 22-24  
1048 January 2007, 2007.

1049 Voigt, S., Wagreeich, M., Surlyk, F., Walaszczyk, I., Ulicny, D., Cech, S., Voigt, T., Wiese, F., Wilmsen,  
1050 M., Niebuhr, B., Reich, M., Funk, H., Michalik, J., Jagt, J. W., Felder, P. J., and Schulf, A. S.:  
1051 Cretaceous, in: The Geology of Central Europe Volume 1: Precambrian and Palaeozoic; Volume 2:  
1052 Mesozoic and Cenozoic, edited by: McCann, T., The Geological Society of London, 923–997,  
1053 <https://doi.org/10.1144/CEV2P.3>, 2008.

1054 Wenting, L., Völkner, E., Minkley, W., and Popp, T.: Zusammenstellung der Materialparameter für  
1055 THM-Modellberechnungen - Ergebnisse aus dem Vorhaben KOSINA, BGR, Hannover, 88 pp.,  
1056 2017.

1057 Zang, A. and Stephansson, O.: Stress Field of the Earth's Crust, Springer Netherlands, Dordrecht, 322  
1058 pp., 2010.

1059 Ziegler, M. and Heidbach, O.: Manual of the Matlab Script Stress2Grid v1.1, 2019a.

1060 Ziegler, M. O. and Heidbach, O.: Matlab Script Stress2Grid v1.1, GitHub [code], 2019b.

1061 Ziegler, M. O., Ziebarth, M., and Reiter, K.: Python Script Apple PY v1.0, GFZ Data Services [code],  
1062 2019.

1063 Ziegler, M. O., Heidbach, O., Reinecker, J., Przybycin, A. M., and Scheck-Wenderoth, M.: A multi-stage  
1064 3-D stress field modelling approach exemplified in the Bavarian Molasse Basin, Solid Earth, 7,  
1065 1365–1382, <https://doi.org/10.5194/se-7-1365-2016>, 2016.

1066 Ziegler, P. A. and Dèzes, P.: Crustal evolution of Western and Central Europe, Geological Society,  
1067 London, Memoirs, 32, 43–56, <https://doi.org/10.1144/GSL.MEM.2006.032.01.03>, 2006.

1068 Zoback, M. D.: Reservoir Geomechanics, Cambridge University Press, Cambridge, 2007.

1069